Testing of hot-finished high strength steel SHS and RHS under combined compression and bending

Xin Meng[1*] and Leroy Gardner[2]

[*] Corresponding author. Tel.: +44 (0)77 5157 9750

E-mail address: xin.meng15@imperial.ac.uk (X. Meng)

[1] Ph.D. Candidate, Department of Civil and Environmental Engineering, Imperial College London, London SW7 2AZ, UK

E-mail address: xin.meng15@imperial.ac.uk

[2] Professor of Structural Engineering, Department of Civil and Environmental Engineering, Imperial College London, London SW7 2AZ, UK

E-mail address: leroy.gardner@imperial.ac.uk

Highlights

- Hot-finished S690 and S770 square and rectangular hollow sections were examined;
- Twelve tensile coupons, five stub columns and 30 short beam-columns were tested;
- Local geometric imperfections were investigated by means of 3D laser-scanning;
- Current Eurocode 3 design provisions were assessed using the experimental data.

Testing of hot-finished high strength steel SHS and RHS under combined compression and bending

Xin Meng*, Leroy Gardner

Department of Civil and Environmental Engineering, Imperial College London, London, UK

* Corresponding author. Tel.: +44 (0)77 5157 9750

E-mail address: xin.meng15@imperial.ac.uk

Abstract

An experimental investigation into the cross-sectional behaviour of hot-finished high strength steel tubular sections, to support the assessment and development of structural design guidance, is presented. Two grades of quenched and tempered high strength steel – S690 and S770 and eight cross-sections – seven square hollow sections (SHS) and one rectangular hollow section (RHS), covering a wide range of local slenderness, were examined. This test programme consisted of twelve tensile coupon tests, five stub column tests and 30 short beam-column tests, with various initial loading eccentricities employed to achieve a spectrum of compression and bending combinations. Local geometric imperfection measurements were carried out on each test specimen using 3D laser-scanning, and a rational approach to analysing the local imperfection distributions using the scanned data was subsequently proposed. Following the experimental study, the current Eurocode 3 cross-section design provisions were evaluated through comparisons with the results from the present research and additional results from the literature. The experimental results and findings from the present study provide a basis for the development of numerical models and the enhancement of existing design methods in the future.

Keywords: cross-section design; digital image correlation (DIC); local buckling; local geometric imperfections; high strength steel; hot-finished sections; rectangular hollow sections (RHS); square hollow sections (SHS); testing; 3D laser-scanning

1. Introduction

High strength steels, characterised by steel grades greater than S460 according to Eurocode 3 (EC3) [1,2], are being increasingly used in the construction industry. Compared to conventional steels, the increased strength and higher strength-to-weight ratio of high strength steels enable the use of smaller and lighter structural components, making them popular in high-rise buildings, long-span applications and offshore structures. High strength steels are also typically superior in terms of economy and sustainability due to savings in the overall material and labour costs and reduction in the consumption of non-renewable resources and carbon emissions [3,4], and are therefore set to feature prominently in the future of structural engineering. The mechanical properties of steels are primarily determined by their chemical composition, heat treatment and manufacturing process, among which heat treatment is of major importance in the production of high strength steels. Three types of heat treatment are commonly employed: normalising (N), quenching and tempering (Q&T) and thermomechanical controlled processing (TMCP). The yield strength of the steels with a normalising heat treatment can be increased up to 460 N/mm^2, while quenching and tempering and thermomechanical controlled processing are often adopted for developing high strength steels with grades higher than S460 [5,6].

The advantages of the tubular sections over open sections, such as high structural efficiency in compression, superior torsional resistance, suitability for concrete infill and aesthetics are well known. High strength steel structural hollow sections offer the combined benefits of both high strength and a tubular profile, and have attracted substantial interest from both industry and researchers. Square and rectangular hollow sections (SHS and RHS), which are among the most commonly used hollow section shapes, are the focus of the present study. High strength steel SHS and RHS are primarily either hot-finished (typically hot-rolled and then quenched and tempered) or cold-formed (typically cold-rolled

and welded from Q&T or TMCP steel sheets); alternatively, sections can also be fabricated by welding four high strength steel plates into a box shape. Despite the increasing popularity of high strength steel SHS and RHS, structural design guidance remains rather limited, and further research into their structural behaviour and design is required. Substantial effort has been devoted to the testing of high strength steel built-up box sections, such as [7–11]. Following the recent emergence of rolled high strength steel SHS and RHS products, a number of experimental studies have been conducted to investigate their structural performance, including those reported in [6,12–14] on hot-finished SHS and RHS and in [15–18] on cold-formed SHS and RHS. In general, test data on hot-finished and cold-formed high strength steel SHS and RHS are still relatively scarce, and further results are considered necessary for the development of safe and efficient design provisions. For hot-finished SHS and RHS in particular, there are no experimental data available thus far on slender (Class 4) cross-sections or rectangular hollow sections under combined compression and bending, and steel grades greater than S690 are yet to be explored; the present study is therefore aimed at addressing this topic.

A comprehensive experimental programme has been conducted on eight hot-finished S690 and S770 SHS and RHS, spanning from Class 1 to 4 according to the slenderness limits specified in prEN 1993-1-1:2018 [1]. This programme comprises twelve tensile coupon tests, five stub column tests on SHS, twenty short beam-column tests on SHS and ten short beam-column tests on RHS. Distributions of local geometric imperfections in the hot-finished sections are investigated by means of 3D laser-scanning, and characterisation of local geometric imperfections from the scanned data is addressed. Subsequent to the experimental work, the existing cross-section design methods given in Eurocode 3 [1,2] are evaluated using the obtained test results, and recommendations for further research are made based on the observations from the present study.

2. Experimental investigation

2.1. General

An experimental programme on the cross-sectional behaviour of hot-finished high strength steel square and rectangular hollow sections has been conducted in the Structures Laboratory at Imperial College London and is presented in this section. Two grades of quenched and tempered steel – S690 and S770 and eight section sizes – seven SHS and one RHS, covering all four cross-section classes according to the slenderness limits in prEN 1993-1-1:2018 [1], were examined. The cross-section sizes, material grades, section IDs and classes are summarised in Table 1, and the chemical compositions and material properties, as stated in the mill certificates, are presented in Tables 2 and 3 respectively. This experimental investigation consisted of twelve tensile coupon tests, five stub column tests and 30 short beam-column tests, along with measurement of geometric imperfections for each specimen. The labelling convention of the test specimens is explained through the following example – RSBC1-2, where R represents the section shape (S and R denote SHS and RHS respectively), SBC represents the test type (TC, SC and SBC denote tensile coupon tests, stub column tests and short beam-column tests respectively), 1 represents the section ID (see Table 1) and 2 represents the test ID in the series (omitted if there was only one test in the series).

2.2. Tensile coupon tests

Tensile coupon tests were initially conducted to obtain the key mechanical properties and full stress-strain responses of the test materials. For hot-rolled SHS and RHS, both flat and corner coupons have been tested in the previous experimental studies [6,19], and the uniformity of the material properties around the cross-section has been confirmed. Therefore, only flat coupon tests were performed in the present study. In total, twelve longitudinal tensile coupon tests were conducted – four extracted from the centre of the four flat faces of the tested S690 SHS 100×100×4 profile and two from the centre of two adjacent flat faces of each of the tested S690 SHS 220×220×8, S770 SHS 120×120×6.3, S770 SHS 180×180×7.1 and S770 SHS 250×250×8 profiles. Material coupon tests on the examined S690 SHS

50×50×5, SHS 90×90×5.6 and RHS 100×50×5.6 profiles were previously conducted and reported in [6], but the results are summarised herein.

The coupon specimens were dimensioned in accordance with EN ISO 6892-1:2016 [20] and machined longitudinally from adjacent faces of the section. The extracted coupons were sand blasted prior to dimension measurements being taken to remove the mill scale from their surfaces, thereby enabling a more accurate determination of the initial cross-sectional area of the parallel length S_0 and the subsequent engineering stress (which is equal to the applied force divided by S_0). A series of overlapping standard gauge lengths equal to $5.65\sqrt{S_0}$ in accordance with EN ISO 6892-1:2016 [20], were marked onto the front and back faces of the coupons to determine the percentage elongation after fracture.

The tensile tests were conducted at room temperature in compliance with EN ISO 6892-1:2016 [20] using an Instron 250 kN hydraulic testing machine. Linear electric strain gauges were used for the measurement of the longitudinal strain up to material yielding. After yielding until fracture, the longitudinal strain field within the parallel length became increasingly non-uniform, and strain gauge readings were no longer representative. Therefore, a video extensometer or Digital Image Correlation (DIC) was employed to measure the average strain over the parallel length. Tests STC3-2 and STC5-2 were monitored using DIC (DIC series), while the remaining tests were carried out with a video extensometer (VE series). For the VE series, a pair of strain gauges were affixed at the centre of the front and back faces of the coupons, with the front face sprayed with black paint. Two white dots were then marked onto the front face at a gauge length of 140 mm within the parallel length such that the relative movement between the two dots could be tracked using the video extensometer, thereby obtaining the average strain over the gauge length. For the DIC series, two strain gauges were attached to the centre of the side faces of the specimens; meanwhile, speckle patterns were applied to the front and back faces of the coupons within the parallel length, and the four-camera StrainMaster DIC system from LaVision, with two cameras employed on each side, was used to monitor the strain distribution over the whole parallel length.

The tensile testing machine was controlled by the crosshead separation rate based on the strain rate over the parallel length. As recommended in EN ISO 6892-1:2016 [20], the strain rate was kept constant at 0.007% s^{-1} up to the yield stress and at 0.025% s^{-1} beyond yielding, with a gradual switch between the two rates to avoid an abrupt change of stress. The applied load and strain gauge readings were recorded using the data acquisition equipment DATASCAN and logged at 0.33-second intervals using the DSLOG software. The axial strain from the video extensometer was recorded at 0.1-second intervals using the software package Blue-hill 2, while the DIC data were recorded at 0.33-second intervals and processed using the dedicated software DaVis 8 [21].

The engineering stress-strain curves obtained from the tensile tests are plotted in Fig. 1, and the averaged material properties for each section, including the Young's modulus E, yield strength f_y, ultimate tensile strength f_u, ultimate strain at the ultimate tensile strength ε_u, and the percentage elongation at fracture over the standard gauge length ε_f are summarised in Table 4. The first stage of the stress-strain curve up to $0.9f_y$ was obtained using the averaged strain from the two strain gauges, while the second stage of the curve until fracture was derived based on the strain calculated from the video extensometer for the VE series or from the DIC data for the DIC series; the procedure of the latter is briefly introduced herein. The recorded images were initially processed using DaVis 8 [21], and the strain distributions over the speckled area were obtained for each frame. The average strain over an initial gauge length of 140 mm, i.e. the same as that adopted for the video extensometer, was calculated and exported, together with the corresponding load values, from the software; these were then used to define the second stage of the stress-strain curve. Upon obtaining the stress-strain relationships, the key material properties were subsequently derived. The yield strength f_y was taken as the average stress on the yield plateau, and the Young's modulus E was taken as the average slope of the stress-strain curve in the elastic range between $0.1f_y$ and $0.5f_y$. The majority of the obtained test stress-strain curves displayed the typical characteristics of hot-rolled steels, with a sharply defined yield point and a yield plateau, followed by strain hardening until fracture. The exceptions to this were Specimens STC5-2, STC7-1 and STC7-2, which generally exhibited a similar response to that described above, but with a slightly rounded transition instead of a well-defined yield point, followed by a slightly inclined yield

plateau. Strain hardening was observed in all tests, but is generally much less significant in high strength steel compared to normal strength steel, as highlighted in Fig. 1. This is also reflected by the relatively low f_u / f_y values in Table 4, which fall into a range between 1.03 and 1.05 and fail to meet the required minimum value of 1.05 in EN 1993-1-12:2007 [2]. The requirement of $\varepsilon_f \geq 10\%$ is satisfied in all cases, but, the measured $\varepsilon_u / \varepsilon_y$ values fluctuate around the target value of 15, and fall below 15 for the S770 SHS 120×120×6.3 and S770 SHS 180×180×7.1 profiles. It should be noted that the measured yield strengths for all the investigated materials are higher than 700 N/mm^2, which are outside the scope of EN 1993-1-12:2007 [2]. The ductility requirements for structural steels will be updated in the next revision of Eurocode 3 – the requirements for steels up to S700 are now specified in prEN 1993-1-1:2018 [1], while those for steels over S700 will be given in the next revision of EN 1993-1-12. The ductility of the tested materials is therefore to be re-evaluated upon full release of the next revision of EC3.

2.3. Local geometric imperfection analysis

Geometric imperfections are inevitably introduced into structural steel products primarily during the manufacturing process, and can significantly influence their structural responses including the onset of buckling, initiation of plasticity and ultimate load-carrying capacity. The distributions of local geometric imperfections may vary between different production routes, material types and section sizes. An investigation of the local geometric imperfections in hot-finished high strength steel SHS and RHS is described in this subsection.

A 3D laser-scanning technique was employed to measure the distribution of local geometric imperfections in each test specimen. Firstly, the specimens were sand blasted to eliminate any mill scale on their surface. The outer surface of the specimens was then scanned using a FARO Design ScanArm and recorded using the 3D scanning software Geomagic Wrap [22]. The scanned data were initially processed in Geomagic Wrap, with operations including noise reduction, removal of unwanted data (e.g. weld spatter) and model alignment; a typical pre-processed 3D model is displayed in Fig. 2. The pre-

processed scanned data were then exported in the form of three-dimensional coordinates and analysed using Matlab [23]. Three types of local geometric imperfections – cross-section imperfections, plate imperfections and longitudinal imperfections, and the corresponding data processing procedures, are discussed herein.

The cross-section imperfection is defined as the out-of-flatness of the flat region of the cross-section, as illustrated by the hatched area in Fig. 3(a) for a typical SHS profile, where c denotes the width of the flat region; a similar definition of local geometric imperfections was adopted in [16]. In order to obtain the cross-section imperfections, the data points within the flat region with a width of c, as highlighted in red in Fig. 2, where $c = H - 2r - 2t$ or $c = B - 2r - 2t$, in which H and B are the height and breadth of the cross-section respectively, r is the inner corner radius, t is the thickness and L is the member length, were initially extracted and imported into Matlab [23]. The point cloud was then aligned to the specified coordinate system, as illustrated in Fig. 4, with the X, Y and Z axes corresponding to the longitudinal, transverse and lateral directions of the plate respectively. For a point $(x_i, y_{i,} z_i)$ on the plate, the corresponding cross-section imperfection $\omega_{l,c,i}$ can be calculated from Eq. (1), where $(x_i, 0, z_{y=0})$ and $(x_i, 0, z_{y=c})$ are the two end points shown in Fig. 4. Hence for the cross-section imperfection, a series of straight lines across the width of the cross-section faces serve as the datum for the imperfection measurements. A typical cross-section imperfection distribution processed from the scanned data is demonstrated in Fig. 5(a), where the positive region (i.e. green to red) represents outward deviations and the negative region (i.e. green to blue) represents inward deviations. The maximum cross-section imperfection amplitude over the whole plane $\omega_{l,c}$ may be used as the local geometric imperfection amplitude of the analysed plate.

$$\omega_{l,c,i} = \left(\frac{z_{y=0} - z_{y=c}}{c} \right) y_i + \left(z_i - z_{y=0} \right) \tag{1}$$

The local geometric imperfection can also be defined at the plate level as the deviation with respect to a fitted flat surface, as illustrated by the hatched area in Fig. 3(b). To analyse the distribution of plate imperfections from the scanned data, the point cloud of the flat region was firstly extracted and imported into Matlab [23] with the same alignment as that shown in Fig. 4. A plane was then fitted to the data

points along the two longitudinal edges (i.e. with $y = 0$ and $y = c$) of the plate to serve as a datum, as described by Eq. (2), where k_1, k_2 and k_3 are the derived constant coefficients; this plane was employed to represent the perfect geometry of the analysed face. The plate imperfection $\omega_{l,p,i}$ at any point (x_i, y_i, z_i) can be calculated using Eq. (3), and the distribution of plate imperfections may be subsequently obtained, as shown in Fig. 5(b). The local geometric imperfection amplitude of the analysed plate may be taken as the maximum amplitude of the plate imperfections $\omega_{l,p}$.

$$z = k_1 x + k_2 y + k_3 \tag{2}$$

$$\omega_{l,p,i} = z_i - \left(k_1 x_i + k_2 y_i + k_3\right) \tag{3}$$

Alternatively, the local geometric imperfection can be defined as the out-of-straightness along a series of longitudinal lines within the flat region of each face, as illustrated in Fig. 3(c), which is referred to as the longitudinal imperfection in the present study. A similar approach to characterising local imperfections was adopted in [19] and [24]. Compared with the previous studies where the local imperfections along only one or several longitudinal lines were measured, the 3D laser-scanning technique enables the local imperfection distribution over the entire flat region to be captured. Along any longitudinal line, e.g. $y = y_i$, a straight line was fitted to the data points to serve as the datum for the imperfection measurements, and the deviations of the points from the fitted line were taken as the local imperfections. A typical longitudinal imperfection distribution processed from the scanned data is presented in Fig. 5(c), and the maximum amplitude over the whole plane $\omega_{l,l}$ may be used to represent the local geometric imperfection amplitude of the analysed plate.

The three approaches to the analysis of local imperfections described above were carried out for all 35 test specimens; in total, 140 data points for each type of local imperfections were derived. The measured imperfection amplitudes are plotted against the corresponding values of plate width c in Fig. 6, together with $\omega_l = c / 200$, as recommended in EN 1993-1-5:2006 [25], where ω_l is the local geometric imperfection amplitude. The data points generally exhibit a linear trend – the plate imperfection data are marginally higher on average than the cross-section imperfection data, while the longitudinal imperfection data lie much lower on average than the other two data sets. Through linear regression

analysis, the cross-section and plate imperfection data points yield the best fit functions $\omega_{l,c} = c/145$ and $\omega_{l,p} = c/135$ respectively, both of which are higher than the recommended value of $\omega_l = c/200$ in EN 1993-1-5:2006 [25], while for the longitudinal imperfection data points, the best fit function is $\omega_{l,pr} = c/300$, which is below the codified value of $\omega_l = c/200$. The measured imperfection data are also compared with the Dawson and Walker models [26], as calibrated by Gardner et al. [19], in Fig. 7(a) and 7(b), where f_{cr} is the plate elastic buckling stress and is calculated from Eq. (4), with the buckling coefficient k_σ taken as 4.0 for an internal element in compression and the Poisson's ratio v taken as 0.3. It is observed from both figures that the measured values are far above the predictive models; this can be partially attributed to the different approaches used for the measurement of imperfections. Note however that the measured imperfection profiles are clearly less onerous, in terms of their influence on local buckling, than elastic local buckling mode shapes, which are typically employed in numerical analyses for representing geometric imperfections. Among the three types of local imperfection definitions described herein, the longitudinal imperfection amplitudes are considered to be the most suitable to be used together with elastic buckling mode shapes in numerical modelling to represent the local geometric imperfections. This is because the longitudinal imperfection reflects the deviation from flatness of the plate in the loading direction, while the other two local imperfection definitions also incorporate out-of-flatness of the plate in the transverse direction, which typically has less influence on the plate buckling behaviour under longitudinal loading. The maximum longitudinal imperfection amplitude for the four flat faces for each specimen is reported in Tables 5 and 7 for stub columns and short beam-columns respectively. Further numerical studies are required to calibrate the predictive model for the local imperfection amplitudes and investigate their influence on the structural performance of hot-rolled SHS and RHS.

$$f_{cr} = \frac{k_\sigma \pi^2 E}{12\left(1-\nu^2\right)}\left(\frac{t}{c}\right)^2 \tag{4}$$

2.4. Stub column tests

Concentric compression tests on stub columns were performed to study the local buckling response and ultimate load-carrying capacity of the cross-sections under axial compression. A total of five stub column tests was conducted, with one test performed on each of the following cross-sections: S690 SHS 100×100×4, S690 SHS 220×220×8, S770 SHS 120×120×6.3, S770 SHS 180×180×7.1 and S770 SHS 250×250×8. For the other profiles examined herein, stub column tests were previously carried out by [6], and were not repeated in this study.

The nominal length of the stub columns was taken as three times the larger nominal dimension of the cross-section [27] to avoid any significant influence from global buckling but still contain a representative pattern of local geometric imperfections and residual stresses. The specimens were cut using a band saw, with the ends machined flat and square to ensure a uniform distribution of stress over the cross-section during testing. Measurements of the geometric dimensions were taken after sand blasting. The average measured dimensions, along with the measured local imperfection amplitudes, are summarised in Table 5, where R and r are the outer and inner corner radii respectively and L is the length.

The compression tests on Specimens SSC3 and SSC5 (i.e. the S690 SHS 100×100×4 and S770 120×120×6.3 profiles respectively) were performed using an Instron 3500 kN hydraulic testing machine (Instron series), while for Specimens SSC4, SSC6 and SSC7 (i.e. the S690 SHS 220×220×8, S770 SHS 180×180×7.1 and S770 SHS 250×250×8 profiles respectively), for which the calculated nominal plastic loads (i.e. Af_y, where A is the cross-sectional area) exceeded 3500 kN, an Enerpac 10 MN machine was used (Enerpac series). The setup and instrumentation for the Instron series are shown in Fig. 8(a). The stub column specimens were loaded between the two parallel end platens of the testing machine, which provided fixed-ended boundary conditions, under displacement control. A spherical bearing was mounted onto the top end platen to eliminate any gaps between the specimens and the bearing plate and therefore ensure a uniform compressive stress distribution. A pair of hardened end plates were placed between the specimen ends and the platen (or spherical bearing) to avoid damage to the test setup due

to high levels of the localised stress. Four strain gauges were affixed to the mid-height of two opposite faces of the cross-sections at a distance of 2.5t from the edges, while four linear variable displacement transducers (LVDTs) were used to measure the vertical displacement between the top and bottom end plates, as illustrated in Fig. 9. For the Enerpac series, the setup and instrumentation are shown in Fig. 8(b). The load was applied using an Enerpac 10 MN CLRG-10006 hydraulic cylinder, which was driven under manual oil pressure rate control, with three 3000 kN load cells affixed at the bottom to measure the applied load during testing. A pair of high strength steel end plates was placed at the ends of the specimens to avoid damage to the hydraulic cylinder and load cells. The top test frame was carefully adjusted prior to each test to eliminate any gaps between the specimen and the cylinder. Four strain gauges and four LVDTs were used to monitor the axial displacement of the specimens, and were arranged in the same location as in the Enerpac series; in addition, a two-camera StrainMaster DIC system from Lavision was employed to monitor the strain development on one face of the tested profiles.

For the Instron series of tests, the machine displacement rate was chosen such that a compressive strain rate of 0.1% min^{-1} was achieved. The load, machine displacement, strain gauge readings and LVDT readings were recorded at 0.5-second intervals using the data acquisition equipment DATASCAN and logged using the DSLOG software. For the Enerpac series of tests, a loading rate equal to 0.001EA min^{-1} was manually maintained to achieve approximately the same strain rate as used in the Instron series in the ascending stage. The oil pressure, load cell readings, strain gauge readings and LVDT readings were recorded at 1.5-second intervals using DATASCAN and logged using the DSLOG software, while the images for the DIC system were recorded at a frequency of 0.5 Hz and processed by DaVis 8 [21].

Failure of all the tested stub columns featured local buckling, with the failure modes shown in Fig. 10. The load-end shortening curves were corrected to eliminate the unwanted elastic deformations of the end platens following the procedure set out in [28,29] and are shown in Fig. 11 in a normalised manner, with the key test results reported in Table 6, where N_u is the ultimate load and δ_u is the end shortening at the ultimate load. It can be observed from Fig. 11 that Specimens SSC3 and SSC5 were capable of

achieving their plastic load $N_{pl} = Af_y$ prior to a loss of load-carrying ability due to the development of local buckling, while for Specimens SSC4, SSC6 and SSC7, which are characterised as Class 4 cross-sections according to prEN 1993-1-1:2018 [1] with values of $c/t\varepsilon$ (where $c = H - 2t - 2r$ and $\varepsilon = \sqrt{235/f_y}$) far beyond the Class 3 slenderness limit, local buckling and cross-section failure occurred before N_{pl} was reached. The DIC results for Specimen SSC6, together with the corresponding load-end shortening curve, are displayed in Fig. 12, where the axial strain ε_{yy} is the strain in the longitudinal direction and the *z*-displacement is the out-of-plane displacement within the monitored flat region. The development of the axial strain field, the formation of local buckling and the deformed shape in the post-ultimate regime can be clearly seen.

2.5. Short beam-column tests

Short beam-column tests were performed to investigate the cross-sectional response and load-carrying capacity under combined compression and bending. In total, 30 compression plus uniaxial bending tests were conducted on the following five selected sections – S690 SHS 50×50×5, S690 SHS 90×90×5.6, S690 SHS 100×100×4, S770 120×120×6.3 and S690 RHS 100×50×5.6. For each SHS profile, five tests with different combinations of compression and bending were performed, while for the RHS 100×50×5.6 profile, ten tests – five with major axis bending and five with minor axis bending – were carried out.

The nominal length of the short beam-columns was set, as for the stub columns, equal to three times the larger nominal dimension of the cross-section. The specimens were cut using a band saw, with both ends machined flat and square after cutting. Prior to the measurement of the geometric properties, the mill scale on the outer surface of the specimens was removed by sand blasting. The average measured dimensions are summarised in Table 7.

All the short beam-columns were tested using an Instron 2000 kN hydraulic testing machine. The test setup and instrumentation are shown in Fig. 13. Pinned-end boundary conditions were achieved through the use of a pair of hardened knife edges, which allowed rotation only about the axis of bending. To

apply compression and bending simultaneously, the test specimens were bolted eccentrically onto the wedge plates through a pair of end plates that were welded to the ends of the specimens. The initial loading eccentricity was varied for each test to achieve a range of compression and bending combinations, as listed in Table 8, where e_n and e_m are the nominal and measured initial loading eccentricities respectively. The end plates were sufficiently thick to prevent any significant deformation during testing, and extra weld material was applied on the tensile side of the specimens to avoid failure due to weld fracture. Note that the local geometric imperfection measurements were carried out after welding of the end plates to ensure that any distortional deformation due to welding was captured. The effective length of the short beam-columns, i.e. the distance between the centres of rotation of the pinned-end supports, was equal to the member length L plus two times the combined thickness of the end plate, wedge plate and knife edge L_{end}; the nominal values of L_{end} are provided in Table 7. Four strain gauges were attached longitudinally at the mid-heights of the compressive and tensile sides of the test specimens at a distance of 2.5t from the edges. An LVDT was located at the mid-height of the specimens on the tensile side for the measurement of lateral deflections to calculate the second-order bending moment. Two inclinometers were mounted onto the top and bottom wedge plates to record the rotations at both ends. A four-camera StrainMaster DIC system from Lavision, with two cameras on the compressive face and the other two on the side face (i.e. the face perpendicular to the axis of bending), was employed for four selected tests to monitor the deformation and strain development.

The eccentric compression tests were conducted under displacement control at a machine displacement rate depending on the member length and initial loading eccentricity such that a compressive strain rate of approximately 0.1% min^{-1} was achieved. The applied load, machine displacement, strain gauge readings, mid-height lateral deflection from the LVDT and end rotation from the inclinometers were recorded at 0.5-second intervals using the data acquisition equipment DATASCAN and logged using the DSLOG software. The DIC images were recorded at a frequency of 0.5 Hz and processed using DaVis 8 [21].

Local buckling featured in the failure modes of all specimens, typical examples of which are shown in Fig. 14, apart from the SSBC1 series for which the behaviour was dominated by material yielding with

no visible local buckling. The test load-mid-height lateral deflection curves and load-end rotation curves are arranged by cross-section and displayed in Fig. 15, while the key test results are reported in Table 8, where N_u is the ultimate load, $M_{tot,u}$ is the corresponding total bending moment at N_u and Δ_u and φ_u are the corresponding mid-height lateral deflection and end rotation at N_u. The total bending moment M_{tot}, as given by Eq. (5), includes the applied first-order bending moment and the second-order bending moment at mid-height due to the lateral deflection. The obtained DIC results for Specimen SSBC5-4 are presented in Fig. 16, where the strain fields, as well as the onset and development of local buckling, can be clearly visualised. The deformed shape of Specimen SSBC 5-4 in the post-ultimate regime is also demonstrated in Fig. 16 in a quantitative manner.

$$M_{tot} = N\left(e_m + \Delta\right) \tag{5}$$

A common approach to defining the ultimate cross-section capacity from short beam-column tests and simulations is to take the maximum axial load and corresponding total bending moment (referred to as the N_{max} approach), as adopted in [14,24,30]. However, this approach may lead to an underestimation of the cross-section resistance, particularly for compact (Class 1 or 2) cross-sections, according to the findings of this study, as described below. For the tested Class 1 and 2 cross-sections, there was no obvious sign of local buckling at the peak axial load and the slight drop in load after the peak (seen in the load-deformation responses in Figs. 15(a), 13(b), 13(d), 13(e) and 13(f)) is attributed primarily to the combined effects of material yielding and global buckling. With increasing lateral deflections, while the axial load is dropping, the second-order bending moment is typically rising, and hence the definition of cross-section failure is ambiguous. This phenomenon is revealed clearly by considering typical normalised axial load-total bending moment histories, as plotted Fig. 17 – after reaching the peak axial load (circled in dotted blue lines), the tested compact cross-sections were still capable of taking further bending moment despite the slight decrease in the axial load. Hence, in order to characterise cross-section failure under combined loading, a normalised load factor R, incorporating both the applied axial compression and bending moment, is defined in Eq. (6) and utilised herein. The R-deformation curves for all the short beam-column tests are plotted in Fig. 18, where the red circle represents the point corresponding to the peak axial load. From the R-deformation curves, it is clear that that the tested Class

1 and 2 section short beam-columns (i.e. those from the SSBC1, SSBC2, and RSBC1 series) were still capable of carrying further bending moment after the peak load had been reached. By plotting the axial load and bending moment at the peak value of R instead of N in Fig. 17 (circled in solid red lines), the limit state corresponding to cross-section failure is accurately captured (referred to as R_{max} approach herein). Note that for Class 3 or 4 sections, this approach generally yields the same results as the N_{max} approach, as shown by the dashed line in Fig. 17. The axial load and corresponding total bending moment at the maximum load factor R are therefore deemed more suitable for representing the cross-section capacity compared to those based on the maximum axial load N; the results of the conducted short beam-column tests obtained from both approaches are summarised in Table 8. The proposed approach based on the load factor R is recommended for the characterisation of cross-section failure and the determination of the cross-section resistance under combined loading.

$$R = \frac{N}{N_{pl}} + \frac{M_{tot}}{M_{pl}} \tag{6}$$

3. Comparisons with codified design methods

3.1. General

In this section, the experimental results generated in the present study, together with existing test data on hot-rolled SHS and RHS collected from the literature, are compared with the resistance predictions from the current design guidance given in Eurocode 3.

3.2. Current design provisions in Eurocode 3

For the case of axial compression, the design cross-section resistance to axial load $N_{c,Rd}$ according to Eurocode 3 is equal to the plastic resistance $N_{pl,Rd}$ (Eq. (7)) for Class 1, 2 and 3 SHS and RHS, and is equal to the effective section resistance $N_{eff,Rd}$ (Eq. (8)) for Class 4 SHS and RHS to account for the occurrence of local buckling prior to yielding, where the subscript Rd denotes the design value of the

resistance, γ_{M0} is the partial factor for the resistance of cross-sections and A_{eff} is the effective area, which is determined in accordance with EN 1993-1-5:2006 [25].

$$N_{c,Rd} = N_{pl,Rd} = \frac{Af_y}{\gamma_{M0}} \text{ for Class 1, 2 and 3 SHS and RHS} \tag{7}$$

$$N_{c,Rd} = N_{eff,Rd} = \frac{A_{eff} f_y}{\gamma_{M0}} \text{ for Class 4 SHS and RHS} \tag{8}$$

For the case of bending, the design cross-section resistance $M_{c,Rd}$ is equal to the plastic moment resistance $M_{pl,Rd}$ for Class 1 and 2 SHS and RHS, the elastic moment resistance $M_{el,Rd}$ or elastic-plastic moment resistance $M_{ep,Rd}$ for Class 3 SHS and RHS and the effective moment resistance $M_{eff,Rd}$ for Class 4 SHS and RHS, as given by Eq. (9) to Eq. (11), where W_{pl} is the plastic section modulus, W_{el} is the elastic section modulus, W_{ep} is the elastic-plastic section modulus and W_{eff} is the effective section modulus, which is determined in accordance with EN 1993-1-5:2006 [25].

$$M_{c,Rd} = M_{pl,Rd} = \frac{W_{pl} f_y}{\gamma_{M0}} \text{ for Class 1 and 2 SHS and RHS} \tag{9}$$

$$M_{c,Rd} = M_{el,Rd} = \frac{W_{el} f_y}{\gamma_{M0}} \text{ or } M_{c,Rd} = M_{ep,Rd} = \frac{W_{ep} f_y}{\gamma_{M0}} \text{ for Class 3 SHS and RHS} \tag{10}$$

$$M_{c,Rd} = M_{eff,Rd} = \frac{W_{eff} f_y}{\gamma_{M0}} \text{ for Class 4 SHS and RHS} \tag{11}$$

For the case of combined compression and uniaxial bending, Class 1 and 2 SHS and RHS are able to reach the fully plastic cross-section capacity, and nonlinear interaction curves between the plastic load $N_{pl,Rd}$ and plastic moment resistance $M_{pl,Rd}$ are therefore adopted, as described by Eq. (12) to Eq. (15), where the subscript *Ed* denotes the design value of the effect of the actions. For Class 3 SHS and RHS, a linear interaction formula between $N_{pl,Rd}$ and $M_{el,Rd}$ or between $N_{pl,Rd}$ and $M_{ep,Rd}$ is used, as given by Eq. (16). For Class 4 SHS and RHS, a linear interaction formula based on the effective section properties, as given by Eq. (17), is employed.

$$\frac{N_{Ed}}{N_{pl,Rd}} + \left(1 - 0.5a_w\right)\frac{M_{y,Ed}}{M_{pl,y,Rd}} \le 1 \text{ but } M_{y,Ed} \le M_{pl,y,Rd} \text{ for Class 1 and 2 SHS and RHS} \tag{12}$$

$$\frac{N_{Ed}}{N_{pl,Rd}} + \left(1 - 0.5a_f\right)\frac{M_{z,Ed}}{M_{pl,z,Rd}} \le 1 \text{ but } M_{z,Ed} \le M_{pl,z,Rd} \text{ for Class 1 and 2 SHS and RHS} \tag{13}$$

$$a_w = \left(A - 2Bt\right)/A \text{ but } a_w \le 0.5 \tag{14}$$

$$a_f = (A - 2Ht)/A \text{ but } a_f \le 0.5 \quad (15)$$

$$\frac{N_{Ed}}{N_{pl,Rd}} + \frac{M_{Ed}}{M_{el,Rd}} \le 1 \text{ or } \frac{N_{Ed}}{N_{pl,Rd}} + \frac{M_{Ed}}{M_{ep,Rd}} \le 1 \text{ for Class 3 SHS and RHS} \quad (16)$$

$$\frac{N_{Ed}}{N_{eff,Rd}} + \frac{M_{Ed}}{M_{eff,Rd}} \le 1 \text{ for Class 4 SHS and RHS} \quad (17)$$

3.3. Assessment of EC3 design provisions

In order to assess the accuracy of the current EC3 design formulae for axial compression, the ultimate loads obtained from the stub column tests, combined with the existing data collected from [6,19,31] on hot-rolled SHS and RHS, are normalised by the EC3 cross-sectional resistance $N_{c,EC3}$ and plotted against the plate slenderness $\overline{\lambda}_p$ in Fig. 19, where $\overline{\lambda}_p$ is defined in accordance with EN 1993-1-5:2006 [25] and is taken as the value of the most slender plate element of the cross-section. The statistical results, including the mean and coefficient of variation (COV) values of $N_u / N_{u,EC3}$, where $N_{u,EC3}$ is equal to $N_{c,EC3}$ in the case of axial compression, are summarised in Table 9. Within the range from Class 1 to 3, an increasing level of conservatism with reducing plate slenderness can be observed from Fig. 19 for both normal strength steel and high strength steel SHS and RHS, which is attributed primarily to the influence of strain hardening. As the plate slenderness approaches the Class 3 limit, a number of normal strength steel data points fall below unity, indicating that the current Class 3 slenderness limit of $c/t\varepsilon = 38$ (i.e. $\overline{\lambda}_p = 0.673$) may be too optimistic. The effective width method in EN 1993-1-5:2006 [25] is shown to be suitable for hot-rolled SHS and RHS, as the majority of the Class 4 data points lie on the safe side. Note generally that for cold-formed and welded box sections, on the other hand, previous studies [10,32] have shown that the effective width method in 1993-1-5:2006 [25] often yields unconservative resistance predictions. These findings require further verification based on additional test and numerical data.

For the case of combined compression and bending, the short beam-column test data obtained in the present study, together with the additional data on the S690 SHS 50×50×5, S690 SHS 90×90×5.6 and S690 RHS 100×50×5.6 profiles from [6,12,14], are normalised by the cross-section plastic load N_{pl} and plastic bending moment M_{pl} and plotted against the corresponding EC3 cross-section interaction curves

(based on the average section properties) in Fig. 20 for SHS and in Fig. 21 for RHS. The mean and COV values of $N_u / N_{u,EC3}$, where N_u and $N_{u,EC3}$ are defined in Fig. 22 for the case of combined loading, are reported in Table 9. It is revealed from the graphical and statistical results that the current plastic bi-linear design curves for Class 1 and 2 SHS and RHS generally provide safe-sided results, despite a relatively high level of scatter in the data points due primarily to the lack of account for strain hardening in the interaction formulae. For Class 3 cross-sections, the data points lie far beyond the Class 3 linear interaction curve even though their local slendernesses are approaching the Class 3 limit, which indicates that the EC3 design formulae may be overly conservative for the Class 3 and 4 hot-rolled SHS and RHS under combined loading.

4. Conclusions

An experimental programme focusing on the cross-sectional behaviour of hot-finished high strength steel square and rectangular hollow sections (SHS and RHS) under axial compression and combined loading has been conducted and reported. Two grades of quenched and tempered high strength steels, i.e. S690 and S770, and eight SHS and RHS profiles, ranging from Class 1 to Class 4, were studied. The programme consisted of twelve tensile coupon tests, five stub column tests, 30 short beam-column tests, as well as measurements of local geometric imperfections for all 35 test specimens. 3D laser-scanning was used to examine the local geometric imperfections, and the derived local imperfection amplitudes were discussed relative to the recommendations of Eurocode 3 and existing predictive models. In terms of defining the ultimate resistances of short beam-columns, a new approach was proposed that considers the combination of axial load and bending moment, in preference to the traditional approach which considers only the peak axis load and the corresponding moment. The traditional approach may lead to an underestimation of the cross-section load-carrying capacity for stocky cross-sections. The experimental data generated in the present study, along with existing test results collected from the literature, were subsequently utilised to assess the Eurocode 3 design provisions for hot-rolled SHS and RHS. The presented comparisons revealed that the current EC3 cross-section design rules generally yield safe-sided capacity predictions for hot-finished high strength steel SHS and RHS, though the accuracy could be improved in future research based on the generation of further experimental and numerical data over a wider range of scenarios.

Acknowledgements

This experimental programme was funded by the Research Fund for Coal and Steel (RFCS) under Grant Agreement No. 709892 (2016). The authors gratefully acknowledge the Skempton Scholarship from Imperial College London for the financial support. The authors would also like to acknowledge Trevor Stickland, Alfredo Olivo, Gordon Herbert, Kareem Monzer and Kei Mintzolli for their assistance during the experiments.

References

[1] European Committee for Standardisation, prEN 1993-1-1:2018 Eurocode 3 — Design of steel structures — Part 1-1: General rules and rules for buildings, 2018. Final document.

[2] European Committee for Standardisation, EN 1993-1-12:2007 Eurocode 3 — Design of steel structures — Part 1-12: Additional rules for the extension of EN 1993 up to steel grades S 700, 2007.

[3] N. Baddoo, Editorial, Proc. Inst. Civ. Eng. Struct. Build. 170 (9) (2017) 619-620.

[4] J.L. Ma, T.M. Chan, B. Young, Tests on high-strength steel hollow sections: a review, Proc. Inst. Civ. Eng. Struct. Build. 170 (9) (2017) 621-630.

[5] International Association for Bridge and Structural Engineering, Use and Application of High-Performance Steels for Steel Structures, International Association for Bridge and Structural Engineering (IABSE), 2005.

[6] J. Wang, S. Afshan, N. Schillo, M. Theofanous, M. Feldmann, L. Gardner, Material properties and compressive local buckling response of high strength steel square and rectangular hollow sections, Eng. Struct. 130 (2017) 297-315.

[7] Nishino F, Ueda Y, Tall L. Experimental investigation of the buckling of plates with residual stresses, Laboratory Report No. 290.3, Fritz Laboratory, Lehigh University, 1966.

[8] T. Usami, Y. Fukumoto, Local and overall buckling of welded box columns, J. Struct. Div.-ASCE 108 (1982) 525-542.

[9] K.J.R. Rasmussen, G.J. Hancock, Plate slenderness limits for high strength steel sections, J. Constr. Steel Res. 23 (1) (1992) 73-96.

[10] G. Shi, W. Zhou, Y. Bai, C. Lin, Local buckling of 460MPa high strength steel welded section stub columns under axial compression, J. Constr. Steel Res. 100 (2014) 60-70.

[11] N. Schillo, M. Feldmann, Interaction of local and global buckling of box sections made of high strength steel, Thin-Walled Struct. 128 (2018) 126-140.

[12] J. Wang, S. Afshan, M. Gkantou, M. Theofanous, C. Baniotopoulos, L. Gardner, Flexural behaviour of hot-finished high strength steel square and rectangular hollow sections, J. Constr. Steel Res. 121 (2016) 97-109.

[13] J. Wang, L. Gardner, Flexural buckling of hot-finished high-strength steel SHS and RHS columns, J. Struct. Eng.-ASCE 143 (6) (2017) 04017028.

[14] M. Gkantou, M. Theofanous, J. Wang, C. Baniotopoulos, L. Gardner, Behaviour and design of high-strength steel cross-sections under combined loading, Proc. Inst. Civ. Eng. Struct. Build. 170 (11) (2017) 841-854.

[15] J.L. Ma, T.M. Chan, B. Young, Material properties and residual stresses of cold-formed high strength steel hollow sections, J. Constr. Steel Res. 109 (2015) 152-165.

[16] J.L. Ma, T.M. Chan, B. Young, Experimental investigation on stub-column behavior of cold-formed high-strength steel tubular sections, J. Struct. Eng.-ASCE 142 (5) (2016) 04015174.

[17] J.L. Ma, T.M. Chan, B. Young, Experimental investigation of cold-formed high strength steel tubular beams, Eng. Struct. 126 (2016) 200-209.

[18] B. Somodi, B. Kövesdi, Residual stress measurements on cold-formed HSS hollow section columns, J. Constr. Steel Res. 128 (2017) 706-720.

[19] L. Gardner, N. Saari, F. Wang, Comparative experimental study of hot-rolled and cold-formed rectangular hollow sections, Thin-Walled Struct. 48 (7) (2010) 495-507.

[20] European Committee for Standardisation, EN ISO 6892-1:2016 Metallic materials — Tensile testing Part 1: Method of test at room temperature, 2016.

[21] Lavision, DaVis 8.4, 2017.

[22] 3D Systems, Inc., Geomagic Wrap 2017, 2017.

[23] The MathWorks, Inc., Matlab R2017b, 2017.

[24] O. Zhao, B. Rossi, L. Gardner, B. Young, Behaviour of structural stainless steel cross-sections under combined loading - Part I: Experimental study, Eng. Struct. 89 (2015) 236-246.

[25] European Committee for Standardisation, EN 1993-1-5:2006 Eurocode 3 — Design of steel structures — Part 1-5: Plated structural elements, 2006.

[26] R.G. Dawson, A.C. Walker. Post-buckling of geometrically imperfect plates. J. Struct. Div.-ASCE 98 (1) (1972) 75-94.

[27] R.D. Ziemian, Guide to Stability Design Criteria for Metal Structures, Sixth ed., New York, John Wiley & Sons, Inc., 2010.

[28] L. Gardner, D.A. Nethercot, Experiments on stainless steel hollow sections-Part 1: Material and cross-sectional behaviour, J. Constr. Steel Res. 60 (9) (2004) 1291-1318.

[29] Centre for Advanced Structural Engineering, Compression Tests of Stainless Steel Tubular Columns, Investigation Report S770, 1990.

[30] I. Arrayago, E. Real, Experimental study on ferritic stainless steel RHS and SHS cross-sectional resistance under combined loading, Structures 4 (2015) 69-79.

[31] J. Nseir, Development of a New Design Method for the Cross-Section Capacity of Steel Hollow Sections (Ph.D. Thesis), University of Liège, 2015.

[32] J.L. Ma, T.M. Chan, B. Young, Design of Cold-Formed High-Strength Steel Tubular Stub Columns, J. Struct. Eng. 144 (6) (2018) 04018063.

Table 1 Overview of tested cross-sections

Cross-section size	Grade	Section ID	Class
-	-	-	-
SHS 50×50×5	S690	1	1
SHS 90×90×5.6	S690	2	1
SHS 100×100×4	S690	3	3 / 4
SHS 220×220×8	S690	4	4
SHS 120×120×6.3	S770	5	2
SHS 180×180×7.1	S770	6	4
SHS 250×250×8	S770	7	4
RHS 100×50×5.6	S690	(R)1	1

Table 2 Chemical compositions of tested cross-sections from mill certificates

Cross-section size	Grade	C	Si	Mn	P	S	Al	Cu	Cr	Ni	Mo	V	Ti	Nb	N	W	B
-	-	%	%	%	%	%	%	%	%	%	%	%	%	%	%	%	%
SHS 50×50×5	S690	0.150	0.280	1.50	0.010	0.0020	0.030	0.020	0.670	0.120	0.210	0.070	0.004	0.031	-	-	0.0003
SHS 90×90×5.6	S690	0.150	0.290	1.53	0.010	0.0010	0.021	0.040	0.690	0.100	0.210	0.060	0.004	0.027	-	-	0.0003
SHS 100×100×4	S690	0.140	0.294	1.53	0.011	0.0024	0.020	0.090	0.678	0.130	0.227	0.060	0.003	0.029	0.0062	0.126	0.0004
SHS 220×220×8	S690	0.160	0.310	1.50	0.010	0.0020	0.025	0.040	0.670	0.100	0.200	0.060	0.004	0.029	0.0049	0.110	0.0003
SHS 120×120×6.3	S770	0.160	0.290	1.53	0.012	0.0020	0.021	0.020	0.670	0.110	0.210	0.060	0.003	0.030	0.0050	0.110	0.0003
SHS 180×180×7.1	S770	0.160	0.280	1.51	0.015	0.0020	0.022	-	0.660	0.100	0.200	0.060	0.004	0.027	0.0046	0.110	0.0004
SHS 250×250×8	S770	0.150	0.300	1.50	0.013	0.0030	0.037	0.020	0.660	0.100	0.210	0.060	0.005	0.027	0.0043	0.110	0.0003
RHS 100×50×5.6	S690	0.140	0.280	1.50	0.011	0.0020	0.022	0.030	0.680	0.100	0.210	0.060	0.004	0.029	-	-	0.0003

Table 3 Material properties of tested cross-sections from mill certificates

Cross-section size -	Grade -	$f_{y,mill}$ N/mm^2	$f_{u,mill}$ N/mm^2	$\varepsilon_{f,mill}$ %
SHS 50×50×5	S690	797	838	22.4
SHS 90×90×5.6	S690	789	825	16.6
SHS 100×100×4	S690	785	819	20.1
SHS 220×220×8	S690	745	778	16.0
SHS 120×120×6.3	S770	860	886	18.7
SHS 180×180×7.1	S770	821	857	15.0
SHS 250×250×8	S770	799	846	16.5
RHS 100×50×5.6	S690	778	822	19.7

Table 4 Average measured material properties of tested cross-sections from tensile coupon tests

Cross-section -	E N/mm^2	f_y N/mm^2	f_u N/mm^2	ε_u %	ε_f %	f_u / f_y -	$\varepsilon_u / \varepsilon_y$ -
S690 SHS 100×100×4	211000	787	826	6.2	17.1	1.049	16.6
S690 SHS 220×220×8	209600	812	845	5.8	16.4	1.041	15.0
S770 SHS 120×120×6.3	206300	859	889	5.7	15.4	1.035	13.8
S770 SHS 180×180×7.1	209300	847	883	6.0	17.1	1.042	14.8
S770 SHS 250×250×8	209200	824	864	6.0	16.2	1.048	15.3
S690 SHS 50×50×5*	204300	759	790	7.5	21.7	1.041	20.8
S690 SHS 90×90×5.6*	205500	774	790	7.4	20.1	1.021	20.1
S690 RHS 100×50×5.6*	209500	777	811	7.4	19.3	1.044	20.0

* Tensile coupon tests conducted and reported in [6].

Table 5 Measured dimensions of stub column specimens

Cross-section	Specimen ID	H	B	R	r	t	L	$\omega_{l,l}$
-	-	mm	mm	mm	mm	mm	mm	mm
S690 SHS 100×100×4	SSC3	100.76	100.05	7.9	4.4	3.99	300.03	0.77
S690 SHS 220×220×8	SSC4	219.92	220.59	11.9	6.6	7.86	659.0	1.96
S770 SHS 120×120×6.3	SSC5	119.00	118.62	9.5	3.8	6.29	360.20	0.40
S770 SHS 180×180×7.1	SSC6	178.94	179.38	10.0	4.0	7.04	540.09	0.69
S770 SHS 250×250×8	SSC7	251.61	247.75	9.3	4.3	7.99	755.8	0.89

Table 6 Summary of stub column test results

Cross-section	Specimen ID	c / $t\varepsilon$	N_u	δ_u	N_u / N_{pl}
-	-		kN	mm	-
S690 SHS 100×100×4	SSC3	38.5	1184.3	1.19	1.002
S690 SHS 220×220×8	SSC4	45.2	4784.7	2.83	0.894
S770 SHS 120×120×6.3	SSC5	30.0	2492.8	3.38	1.050
S770 SHS 180×180×7.1	SSC6	42.4	4041.1	2.34	1.000
S770 SHS 250×250×8	SSC7	53.2	5634.8	2.66	0.892

Table 7 Measured dimensions of short beam-column specimens

Cross-section	Specimen ID	H	B	R	r	t	L	L_{end}	$\omega_{l,l}$
-	-	mm	mm	mm	mm	mm	mm	mm	mm
S690 SHS 50×50×5	SSBC1-1	50.16	49.87	6.2	2.8	4.90	149.75	92	0.08
	SSBC1-2	50.12	49.88	5.9	2.6	4.88	149.73	92	0.11
	SSBC1-3	50.12	49.91	6.3	3.0	4.89	148.64	95	0.12
	SSBC1-4	50.21	49.98	5.9	2.7	4.92	149.80	100	0.14
	SSBC1-5	50.12	50.01	6.3	3.0	4.93	149.56	100	0.13
S690 SHS 90×90×5.6	SSBC2-1	89.69	89.43	10.7	4.3	5.70	268.63	95	0.21
	SSBC2-2	89.60	89.96	10.7	4.7	5.85	269.78	100	0.21
	SSBC2-3	90.00	89.78	10.4	4.7	5.72	268.92	105	0.24
	SSBC2-4	89.41	89.80	10.6	4.3	5.70	269.59	105	0.15
	SSBC2-5	89.43	89.69	10.5	4.7	5.75	269.41	105	0.21
S690 SHS 100×100×4	SSBC3-1	100.45	100.06	7.6	4.4	3.94	299.86	95	0.36
	SSBC3-2	100.27	100.35	7.6	4.7	3.98	300.32	95	0.72
	SSBC3-3	100.36	100.19	7.8	4.5	4.01	300.35	100	0.24
	SSBC3-4	100.53	100.26	7.5	4.8	4.01	305.22	105	0.37
	SSBC3-5	100.39	100.15	7.9	4.6	4.00	300.01	105	0.40
S770 SHS 120×120×6.3	SSBC5-1	118.61	118.33	9.8	3.8	6.31	367.60	95	0.20
	SSBC5-2	118.60	118.47	9.7	3.5	6.29	367.68	105	0.35
	SSBC5-3	118.71	118.67	9.6	4.1	6.25	366.88	110	0.30
	SSBC5-4	118.80	118.69	9.9	3.5	6.29	366.45	115	0.34
	SSBC5-5	118.88	119.14	9.8	3.9	6.25	365.07	115	0.54

Table 7 Measured dimensions of short beam-column specimens (continued)

Cross-section	Specimen ID	H	B	R	r	t	L	L_{end}	$\omega_{l,l}$
-	-	mm	mm	mm	mm	mm	mm	mm	mm
S690 RHS 100×50×5.6 ($N + M_y$)	RSBC1-1	100.27	49.34	8.6	4.8	5.62	299.75	92	0.45
	RSBC1-2	100.60	49.35	8.4	4.9	5.64	298.60	95	0.35
	RSBC1-3	100.49	49.44	8.5	4.9	5.60	299.95	100	0.44
	RSBC1-4	100.50	49.11	8.7	4.8	5.62	300.26	105	0.14
	RSBC1-5	100.34	49.13	8.6	4.8	5.62	298.88	105	0.31
S690 RHS 100×50×5.6 ($N + M_z$)	RSBC1-6	100.45	49.56	9.2	5.1	5.63	299.19	92	0.27
	RSBC1-7	100.72	49.24	9.2	4.9	5.64	299.89	95	0.12
	RSBC1-8	100.42	49.30	8.6	4.9	5.63	299.37	95	0.34
	RSBC1-9	100.48	49.47	8.6	5.0	5.61	299.57	100	0.39
	RSBC1-10	100.45	49.42	8.6	4.8	5.63	300.01	100	0.34

Table 8 Summary of short beam-column test results

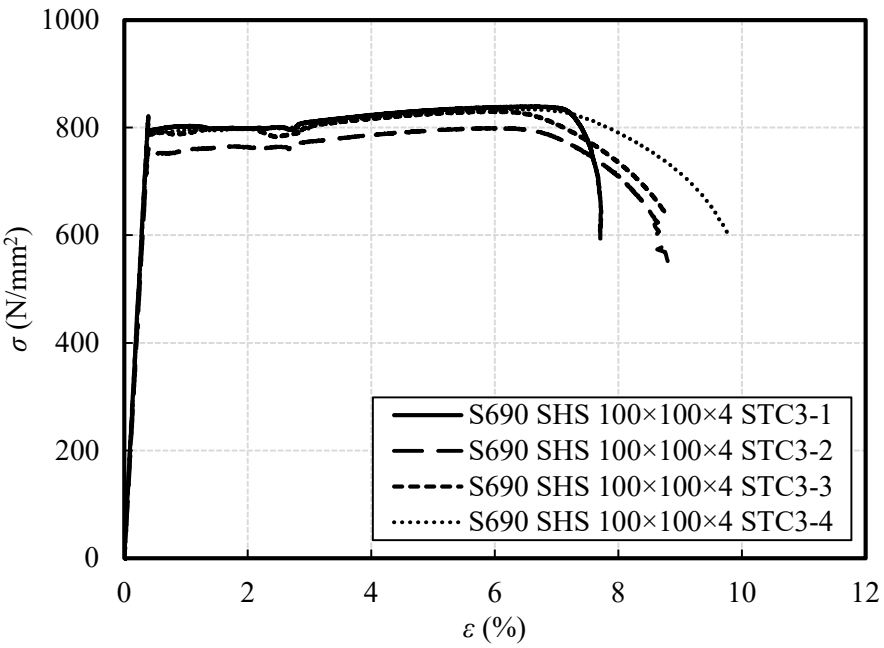
				Criterion: peak load (N_{max} approach)				Criterion: cross-section failure (R_{max} approach)			
Cross-section	Specimen ID	e_n	e_m	N_u	$M_{tot,u}$	Δ_u	φ_u	N_u	$M_{tot,u}$	Δ_u	φ_u
-	-	mm	mm	kN	kNm	mm	°	kN	kNm	mm	°
S690 SHS 50×50×5	SSBC1-1	3	3.40	592.7	2.71	1.17	0.51	458.8	9.51	17.32	7.60
	SSBC1-2	16	16.37	366.8	8.06	5.60	2.63	337.3	10.93	16.04	7.41
	SSBC1-3	35	35.57	250.0	10.39	6.00	2.67	233.9	12.01	15.78	7.12
	SSBC1-4	60	60.20	168.0	11.00	5.29	2.38	161.7	12.43	16.68	7.52
	SSBC1-5	120	118.32	92.0	11.74	9.24	4.30	92.0	11.74	9.24	4.30
S690 SHS 90×90×5.6	SSBC2-1	15	14.85	1035.5	18.16	2.69	0.96	1018.1	22.38	7.14	2.48
	SSBC2-2	20	20.35	973.0	22.31	2.59	0.96	955.1	26.40	7.29	2.52
	SSBC2-3	50	50.00	649.3	37.59	7.89	2.69	647.8	38.15	8.90	3.02
	SSBC2-4	85	85.54	448.0	42.07	8.36	2.85	447.2	42.60	9.72	3.31
	SSBC2-5	175	175.19	240.4	44.19	8.61	3.22	240.0	44.34	9.55	3.57
S690 SHS 100×100×4	SSBC3-1	5	5.17	1049.9	5.99	0.54	0.25	1049.9	5.99	0.54	0.25
	SSBC3-2	10	9.27	950.5	9.69	0.93	0.32	950.5	9.69	0.93	0.32
	SSBC3-3	25	25.01	753.8	20.36	1.99	0.70	753.8	20.36	1.99	0.70
	SSBC3-4	50	50.44	517.0	27.38	2.52	0.84	517.0	27.38	2.52	0.84
	SSBC3-5	90	90.93	343.9	32.23	2.78	0.91	343.9	32.23	2.78	0.91
S770 SHS 120×120×6.3	SSBC5-1	15	15.59	1896.5	33.98	2.32	0.77	1888.1	34.89	2.89	0.93
	SSBC5-2	25	26.95	1615.4	50.91	4.56	1.34	1612.0	51.41	4.94	1.28
	SSBC5-3	35	37.21	1415.3	59.10	4.55	1.29	1412.4	59.51	4.93	1.39
	SSBC5-4	50	50.71	1215.7	67.56	4.86	1.36	1214.9	67.63	4.95	1.39
	SSBC5-5	80	81.69	915.2	80.28	6.02	1.67	915.2	80.37	6.12	1.70

Table 8 Summary of short beam-column test results (continued)

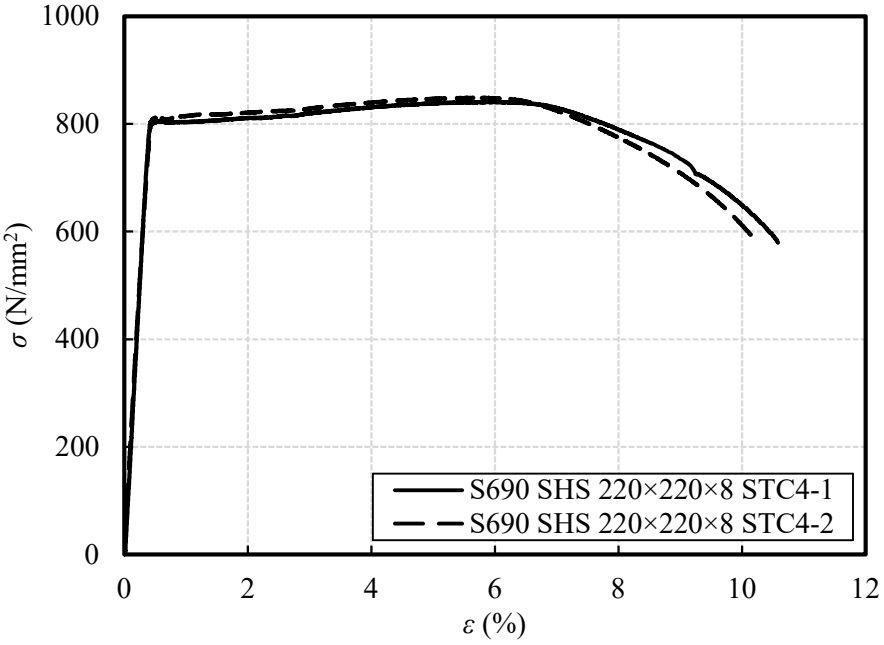
				Criterion: peak load (N_{max} approach)				Criterion: cross-section failure (R_{max} approach)			
Cross-section	Specimen ID	e_n	e_m	N_u	$M_{tot,u}$	Δ_u	φ_u	N_u	$M_{tot,u}$	Δ_u	φ_u
-	-	mm	mm	kN	kNm	mm	°	kN	kNm	mm	°
S690 RHS 100×50×5.6 ($N + M_y$)	RSBC1-1	5	4.70	1091.1	6.01	0.81	0.33	1007.8	12.68	7.89	2.45
	RSBC1-2	15	14.58	861.5	14.97	2.79	0.93	843.8	21.63	11.05	3.55
	RSBC1-3	30	29.10	704.0	27.45	9.89	3.16	678.2	32.62	18.99	5.88
	RSBC1-4	65	65.23	445.9	32.79	8.31	2.60	431.2	37.79	22.40	6.89
	RSBC1-5	180	178.96	195.2	38.65	19.06	6.67	194.1	39.65	25.32	8.93
S690 RHS 100×50×5.6 ($N + M_z$)	RSBC1-6	3	3.49	1030.6	4.94	1.31	0.46	876.0	9.05	6.85	2.16
	RSBC1-7	10	10.71	750.6	9.66	2.17	0.78	652.0	13.37	9.80	3.11
	RSBC1-8	20	19.97	554.7	13.17	3.77	1.30	508.0	15.85	11.23	3.61
	RSBC1-9	45	45.06	331.7	17.72	8.35	2.82	328.2	18.21	10.43	3.44
	RSBC1-10	110	107.97	175.9	20.62	9.25	3.27	175.4	20.71	10.09	3.55

Table 9 Comparisons of test data with EC3 design resistances

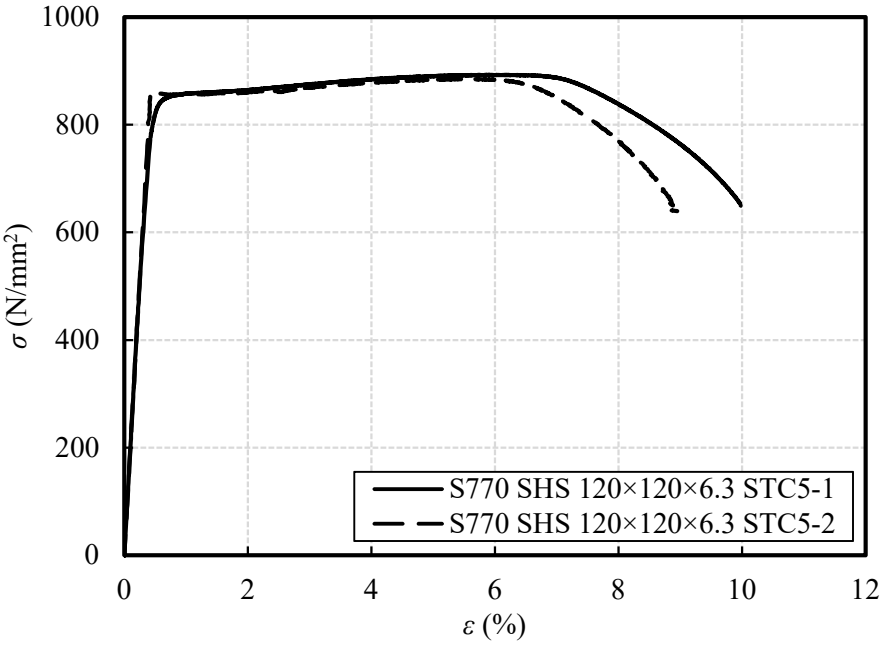
Loading scenario	Evaluation parameter	Class 1 & 2 $N_u / N_{u,EC3}$	Class 3 $N_u / N_{u,EC3}$	Class 4 $N_u / N_{u,EC3}$
N	Mean	1.136		1.023
	COV	0.131		0.083
$N + M$	Mean	1.115	1.162	-
	COV	0.079	0.072	-



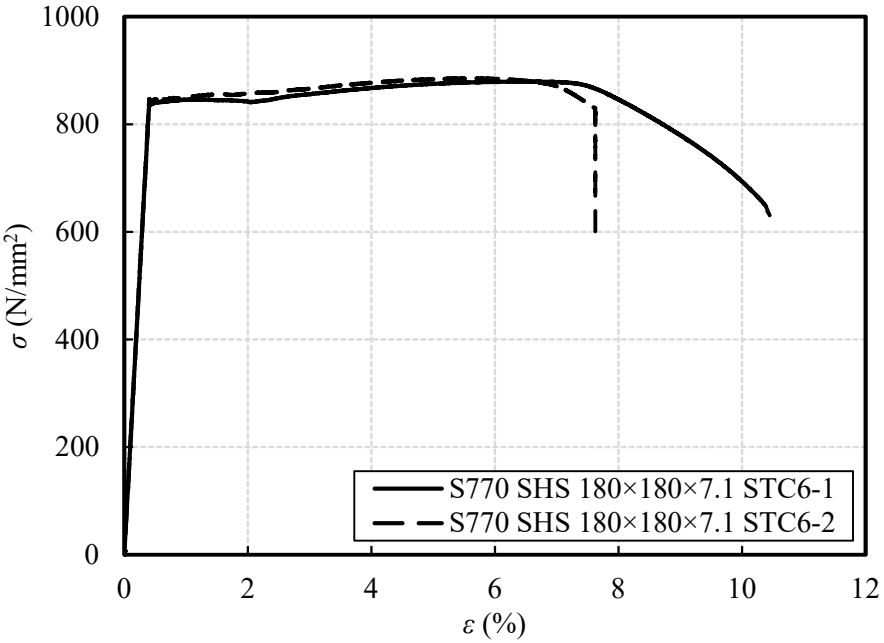
(a) S690 SHS 100×100×4



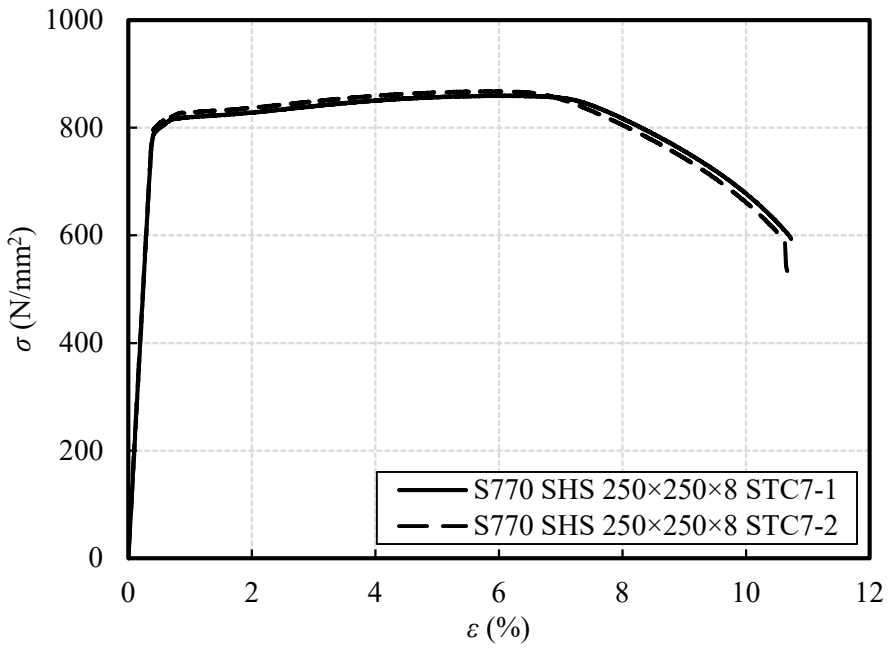
(b) S690 SHS 220×220×8



(c) S770 SHS 120×120×6.3



(d) S770 SHS 180×180×7.1



(e) S770 SHS 250×250×8

Fig. 1. Engineering stress-strain curves obtained from tensile coupon tests on (a) S690 SHS 100×100×4; (b) S690 SHS 220×220×8; (c) S770 SHS 120×120×6.3; (d) S770 SHS 180×180×7.1 and (e) S770 SHS 250×250×8 profiles

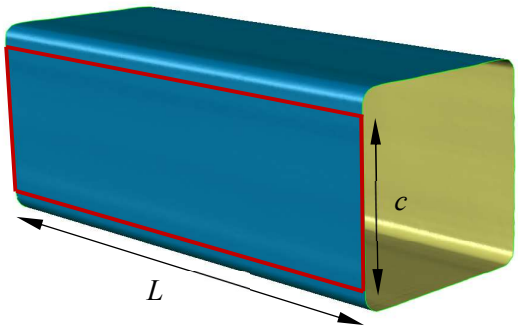
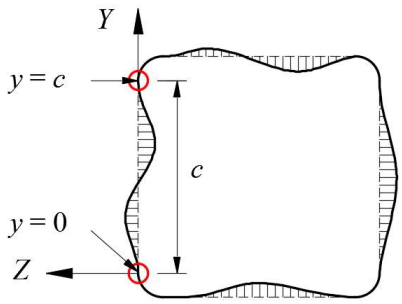
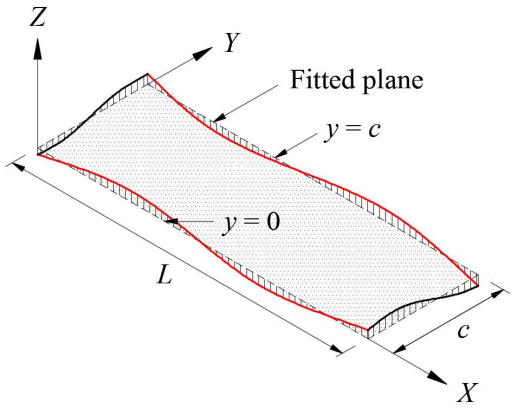


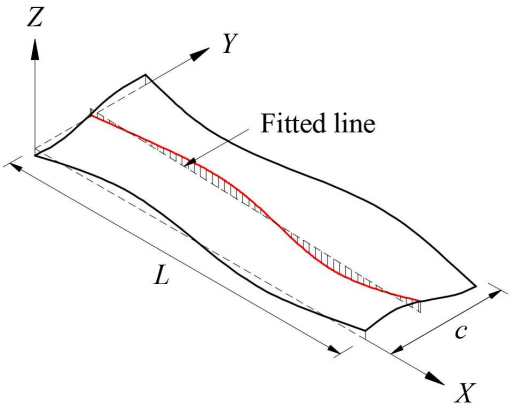
Fig. 2. Typical pre-processed scanned data from Geomagic Wrap



(a) Cross-section imperfection



(b) Plate imperfection



(c) Longitudinal imperfection

Fig. 3. Definitions of (a) cross-section imperfection, (b) plate imperfection and (c) longitudinal imperfection

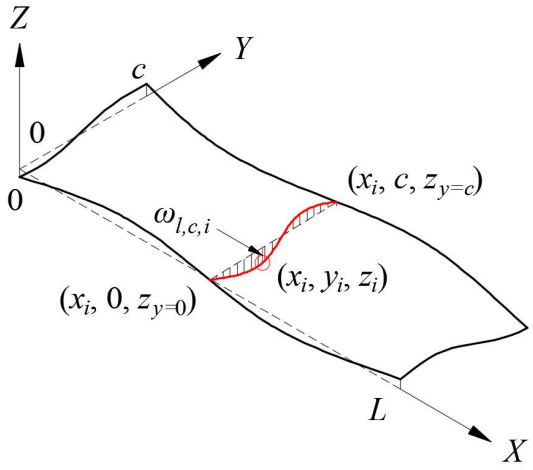
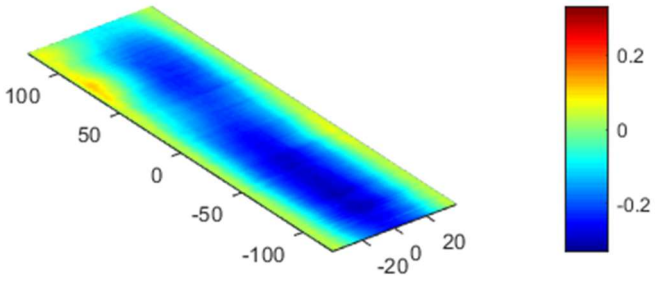
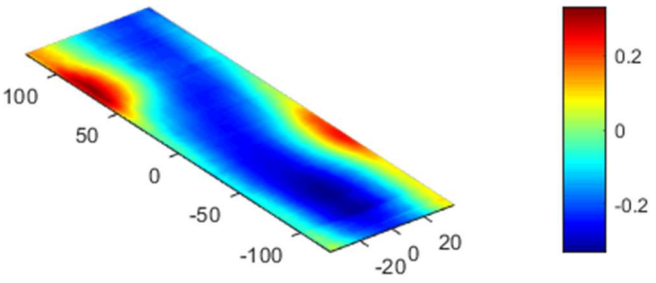


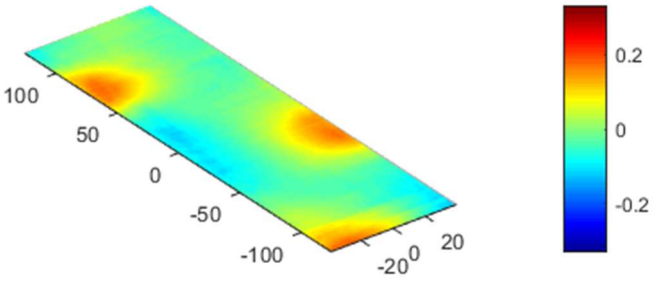
Fig. 4. Determination of cross-section imperfections



(a) Cross-section imperfections



(b) Plate imperfections



(c) Longitudinal imperfections

Fig. 5. Distributions of (a) cross-section imperfections, (b) plate imperfections and (c) longitudinal imperfections for a typical plate (in mm)

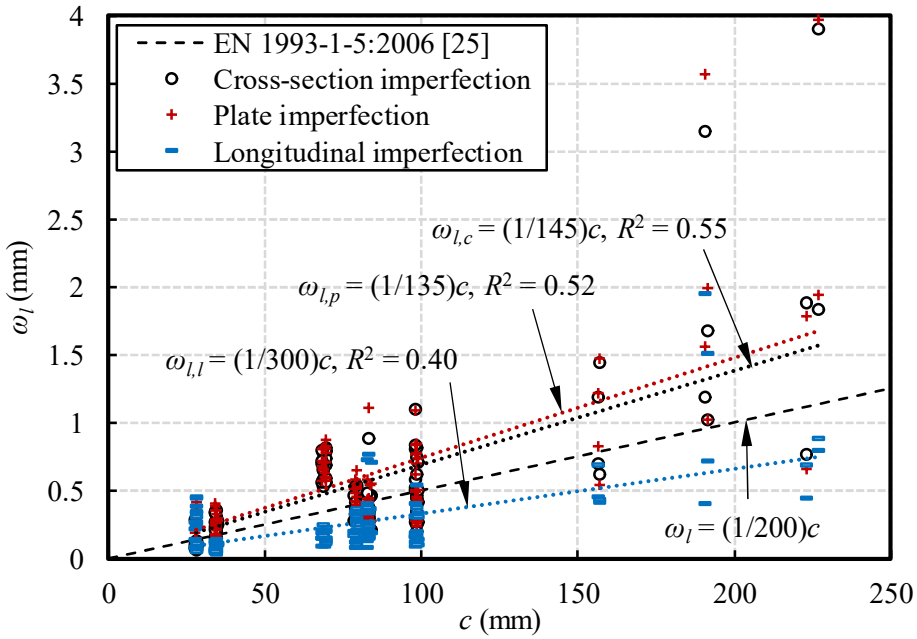


Fig. 6. Comparisons of measured local imperfection amplitudes with recommended values in EN 1993-1-5:2006 [25]

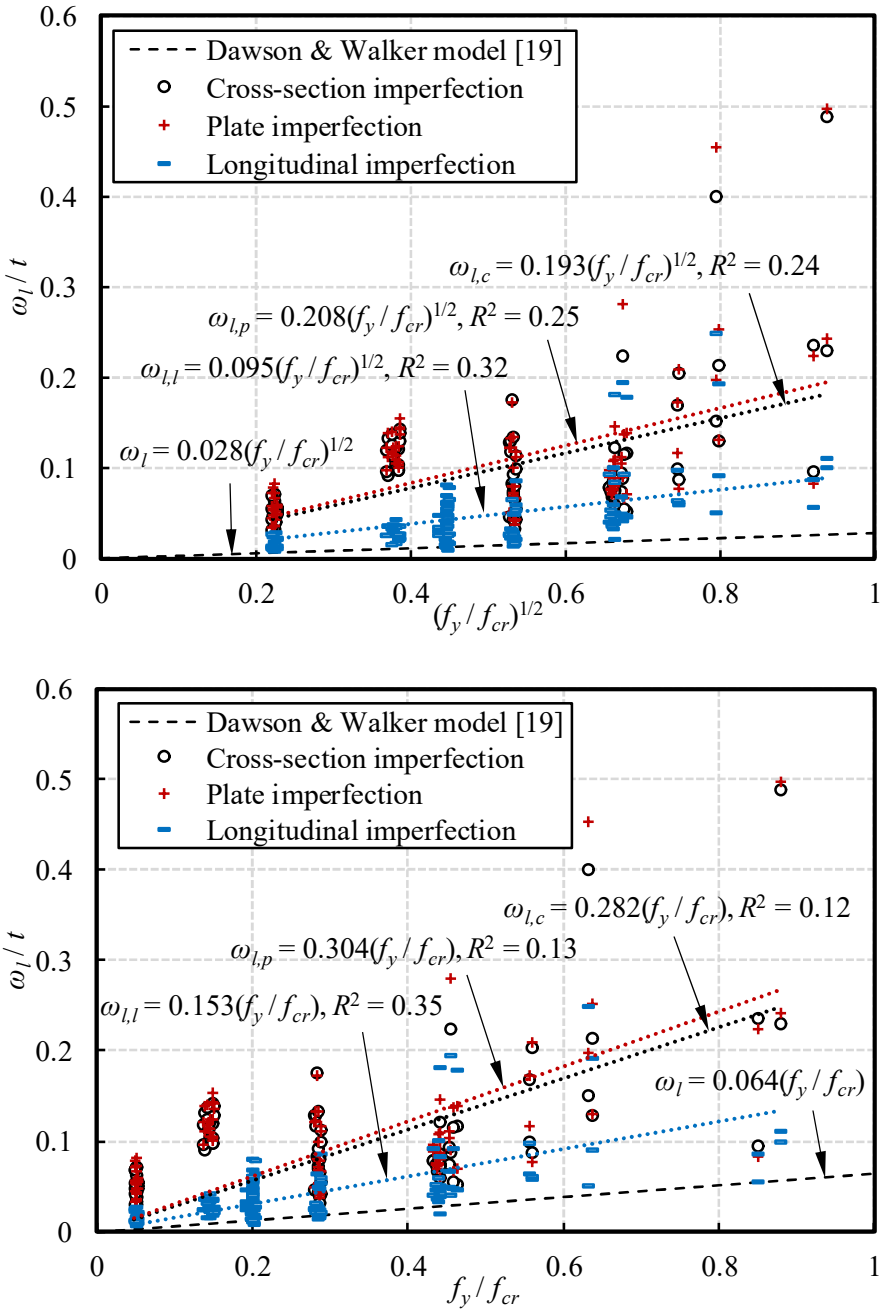
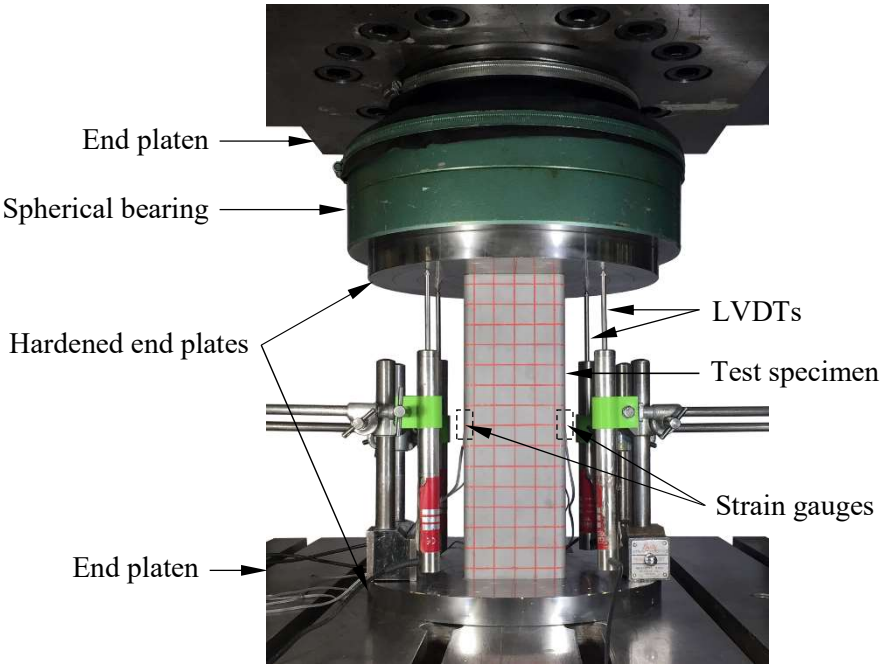
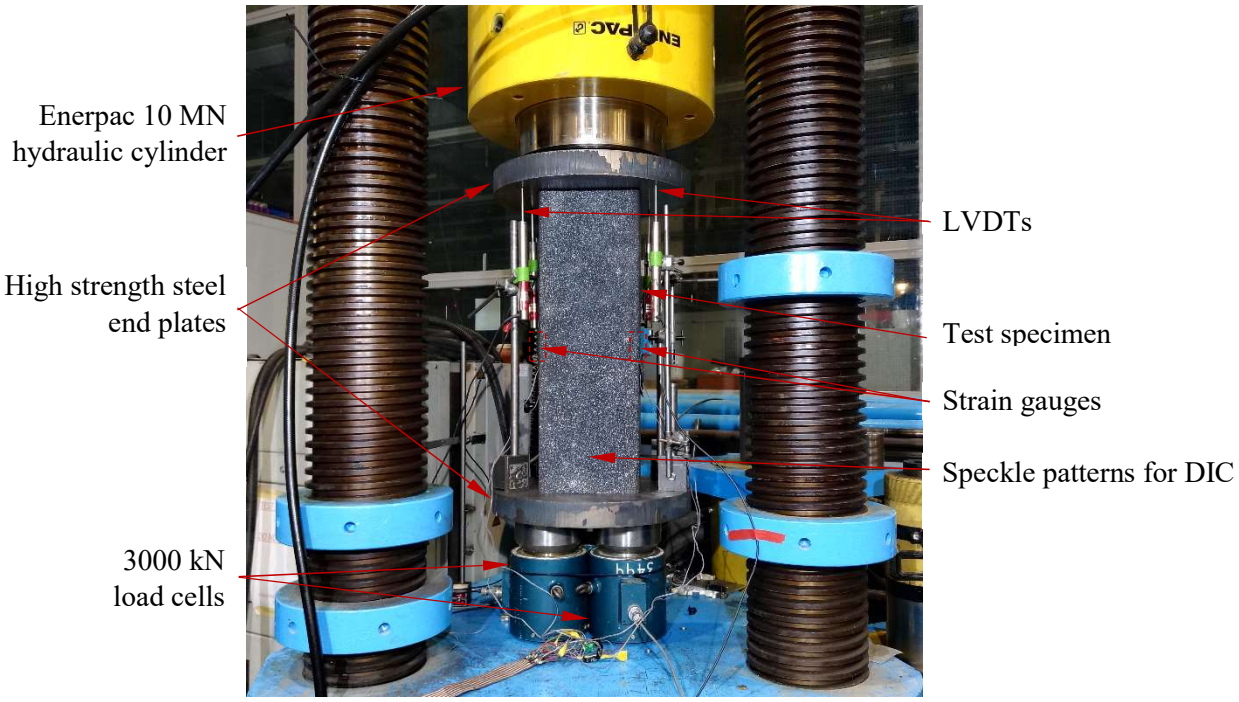


Fig. 7. Comparisons of measured local imperfection amplitudes with existing predictive models



(a) Test setup – Instron series



(b) Test setup – Enerpac series

Fig. 8. Stub column test setup for (a) Instron series and (b) Enerpac series

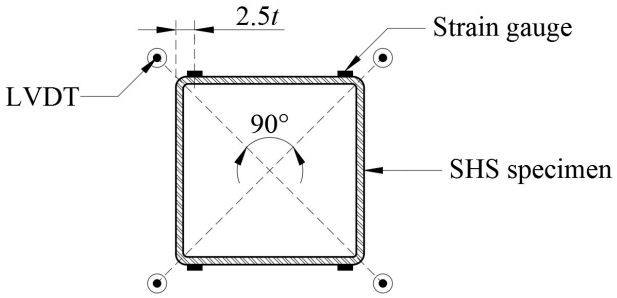
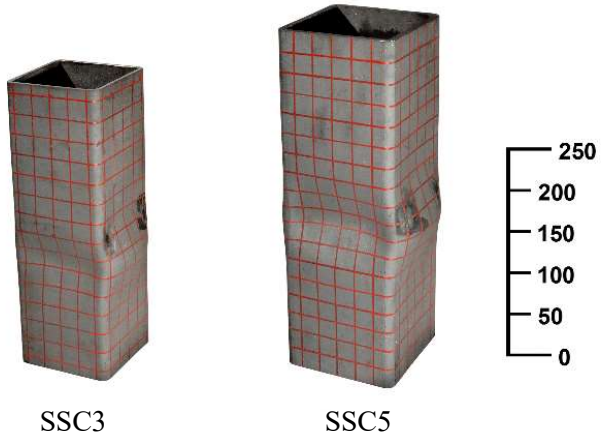


Fig. 9. Arrangement of strain gauges and LVDTs for stub column tests



(b) Failure modes – Instron series



(b) Failure modes – Enerpac series

Fig. 10. Failure modes of stub columns (scales in mm) for (a) Instron series and (b) Enerpac series

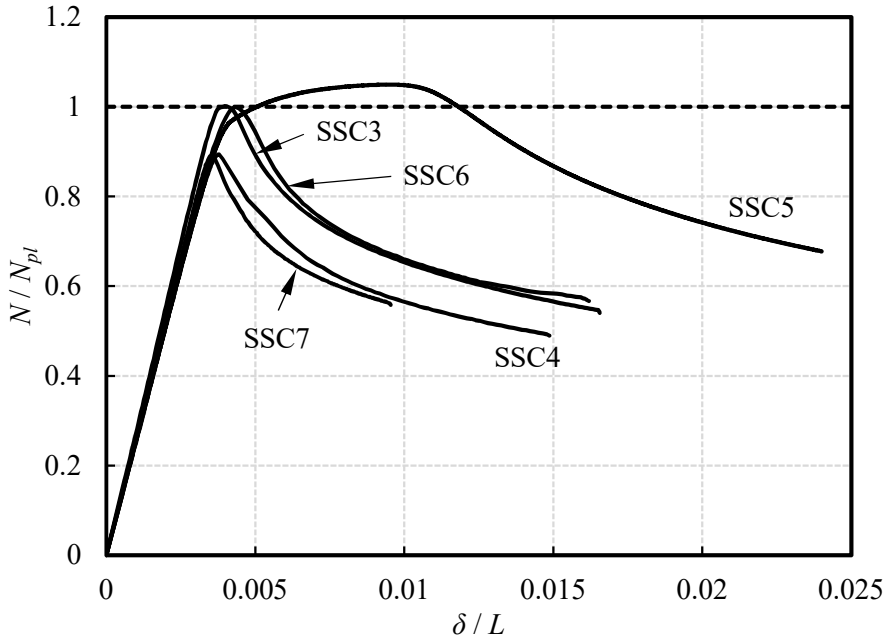


Fig. 11. Normalised load-end shortening curves for stub column tests

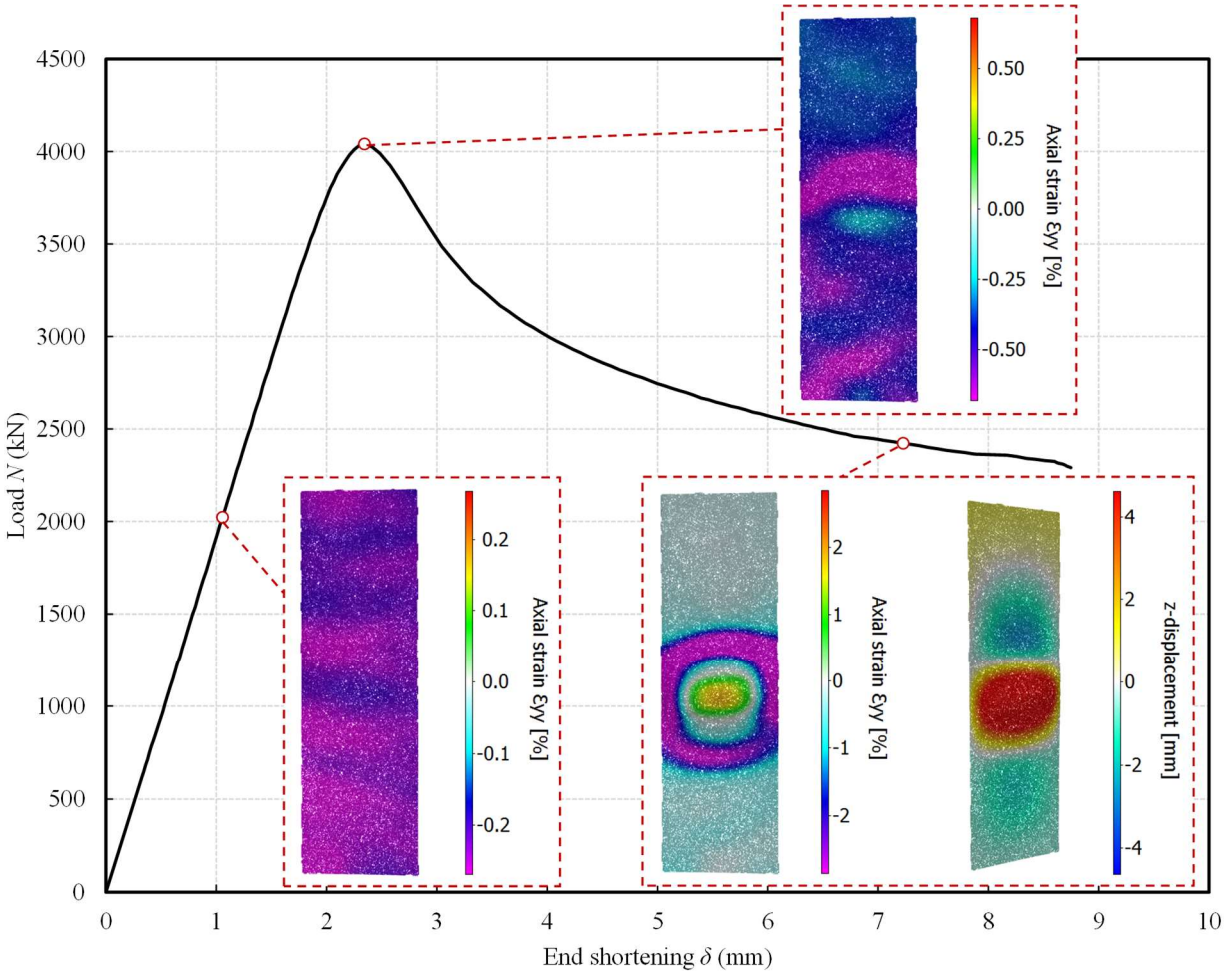


Fig. 12. Typical DIC results for stub column test (SSC6)

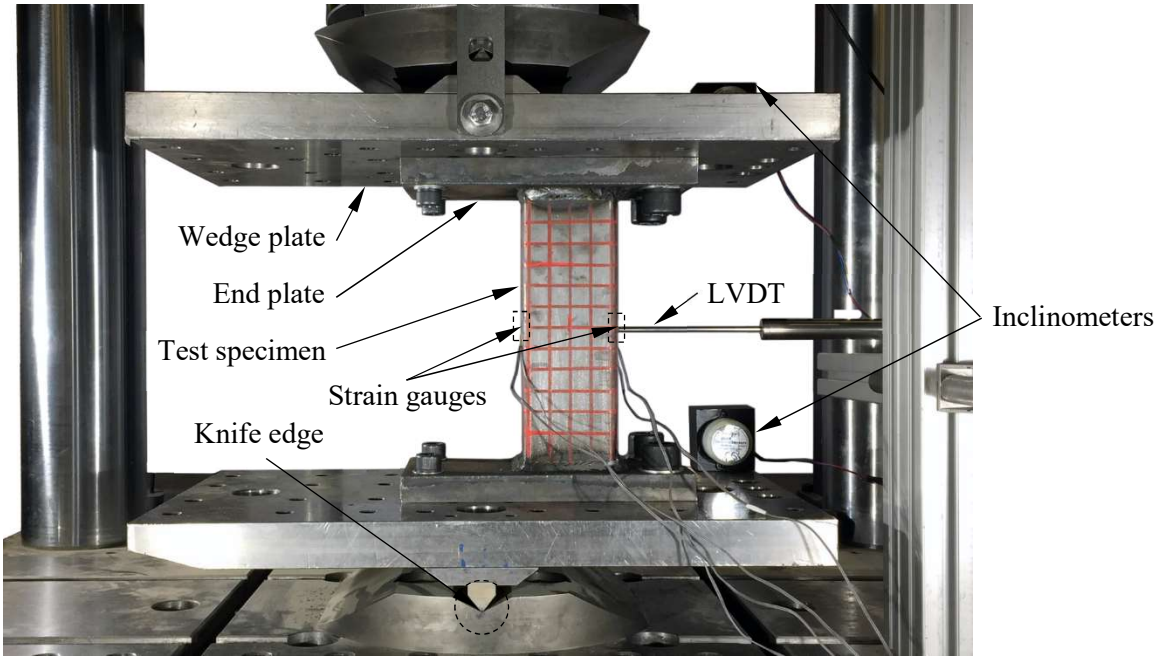


Fig. 13. Short beam-column test setup



(a) S770 SHS 120×120×6.3, e_n = 35 mm (SSBC5-3)

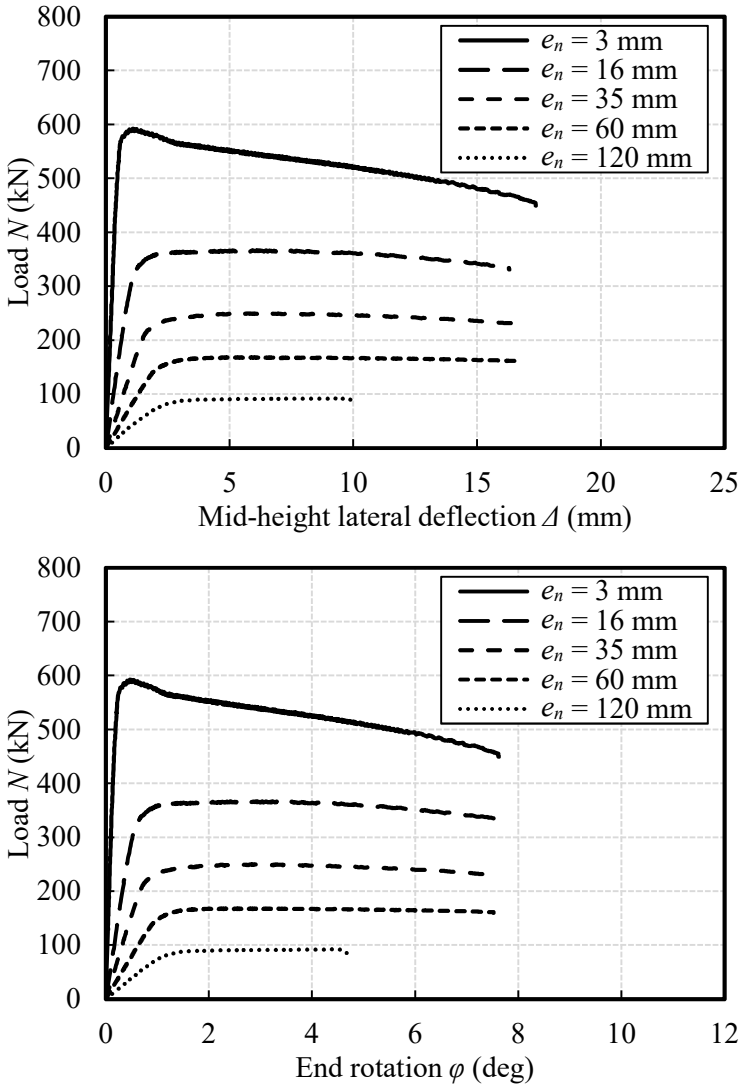


(b) S690 RHS 100×50×5.6, $e_{y,n}$ = 30 mm (RSBC1-3)

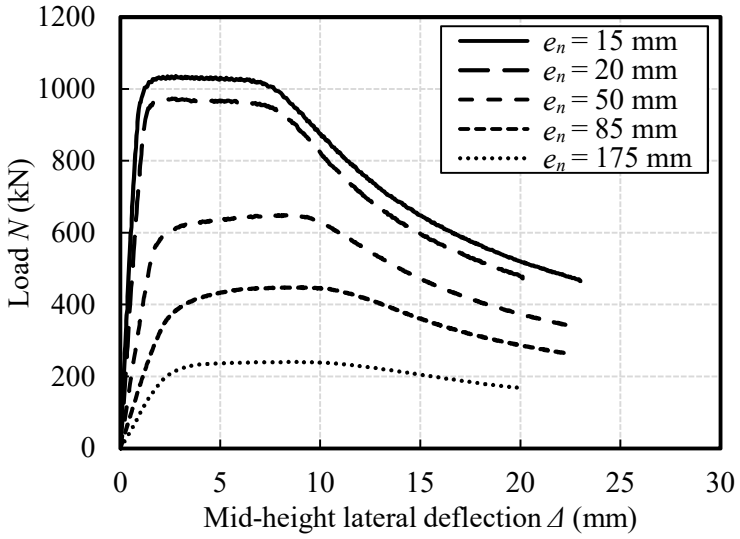


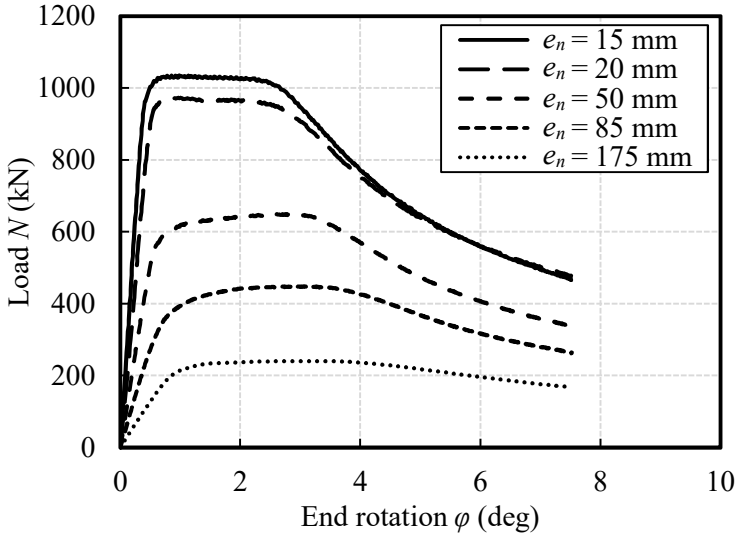
(c) S690 RHS 100×50×5.6, $e_{z,n}$ = 20 mm (RSBC1-8)

Fig. 14. Typical failure modes of short beam-columns (scales in mm) for (a) S770 SHS 120×120×6.3, e_n = 35 mm; (b) S690 RHS 100×50×5.6, $e_{y,n}$ = 30 mm and (c) S690 RHS 100×50×5.6, $e_{z,n}$ = 20 mm

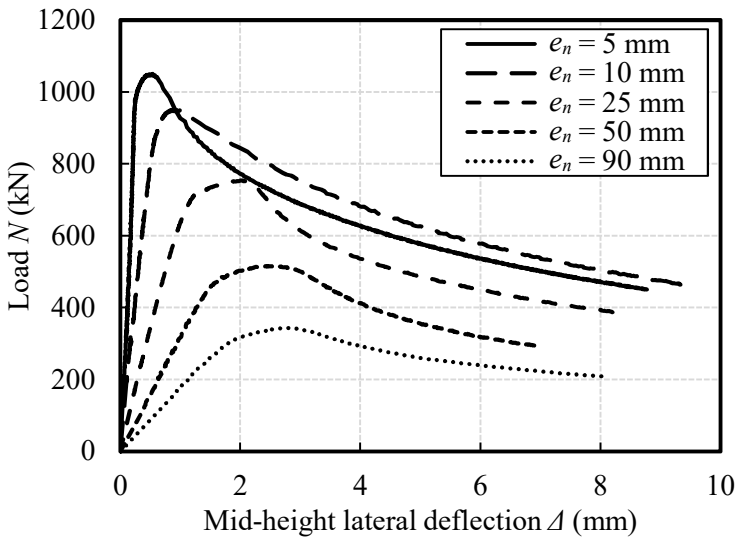


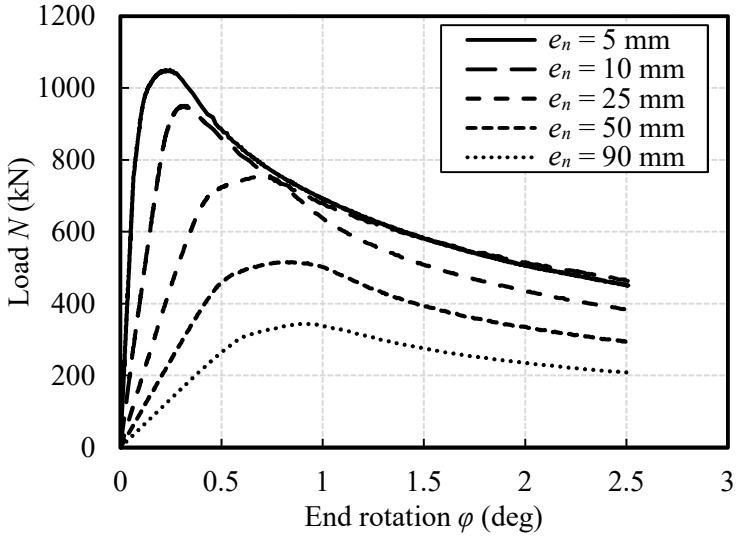
(a) S690 SHS 50×50×5 (SSBC1)



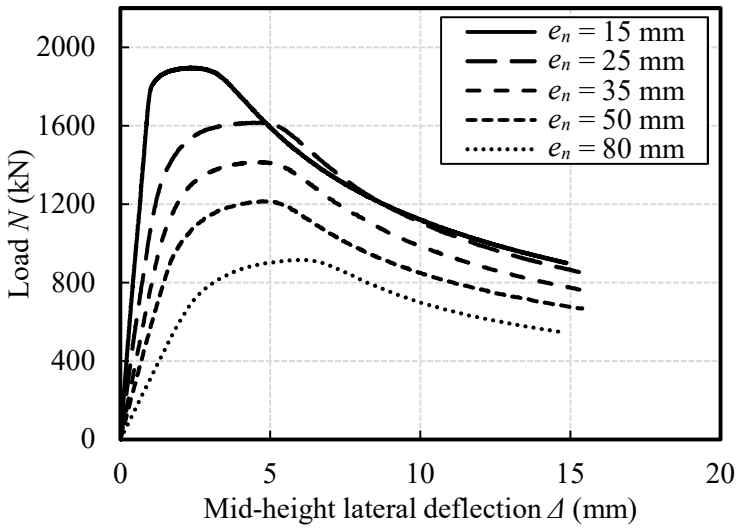


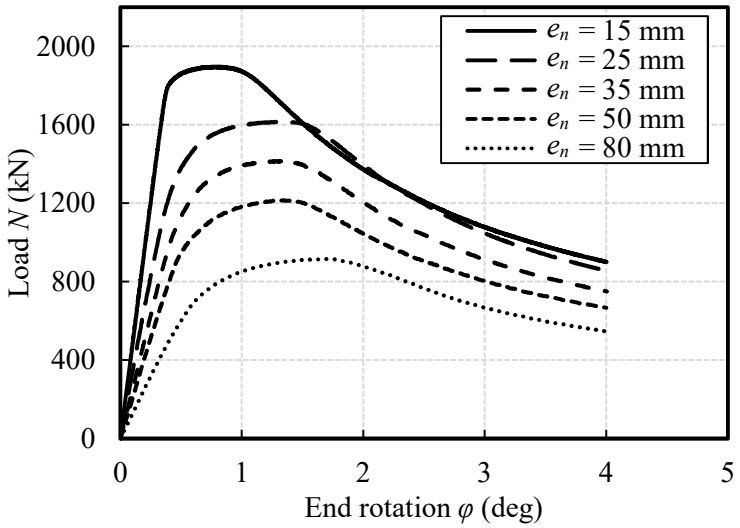
(b) S690 SHS 90×90×5.6 (SSBC2)



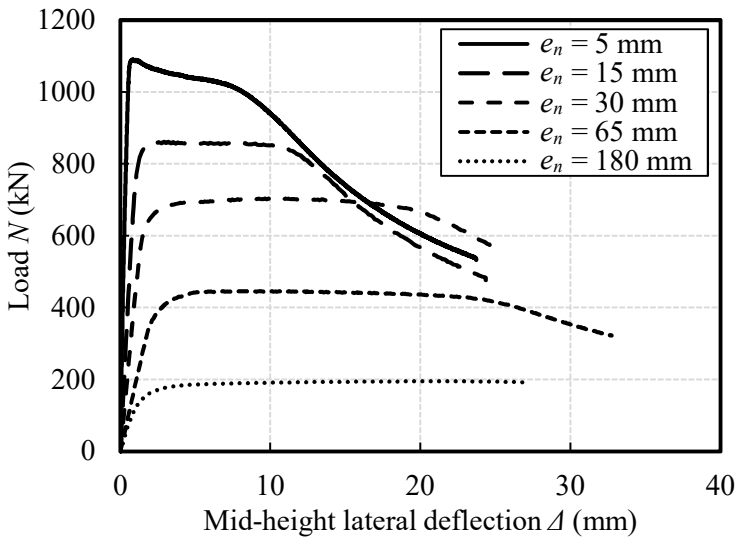


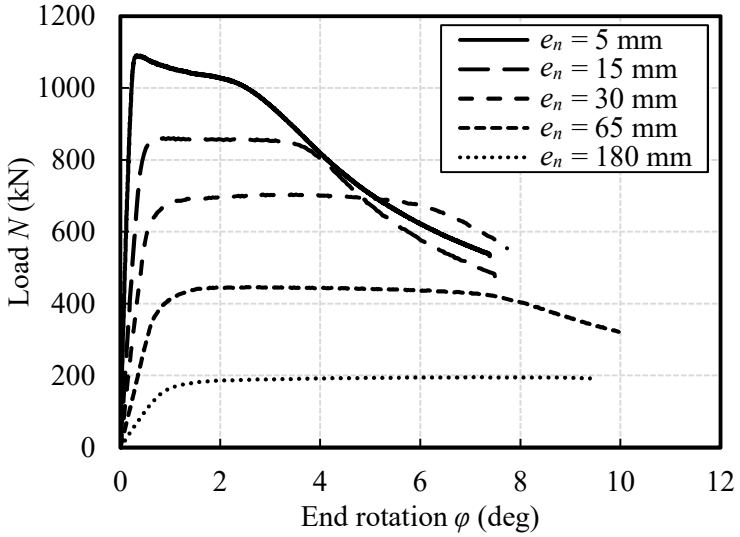
(c) S690 SHS 100×100×4 (SSBC3)



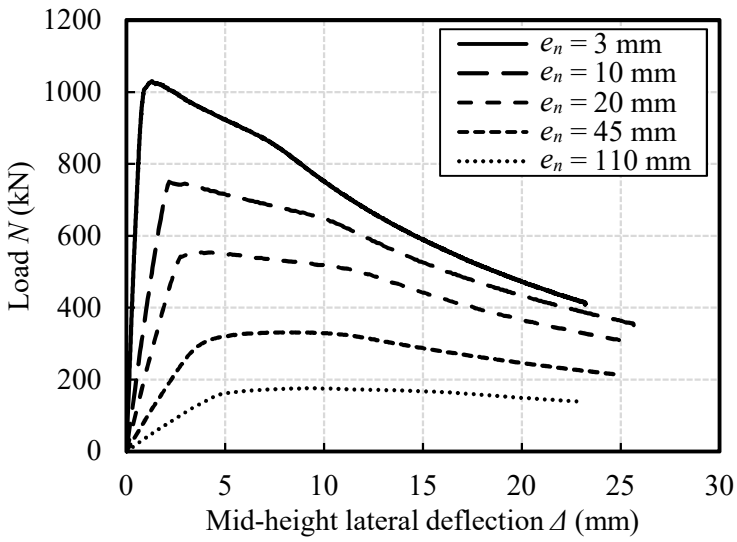


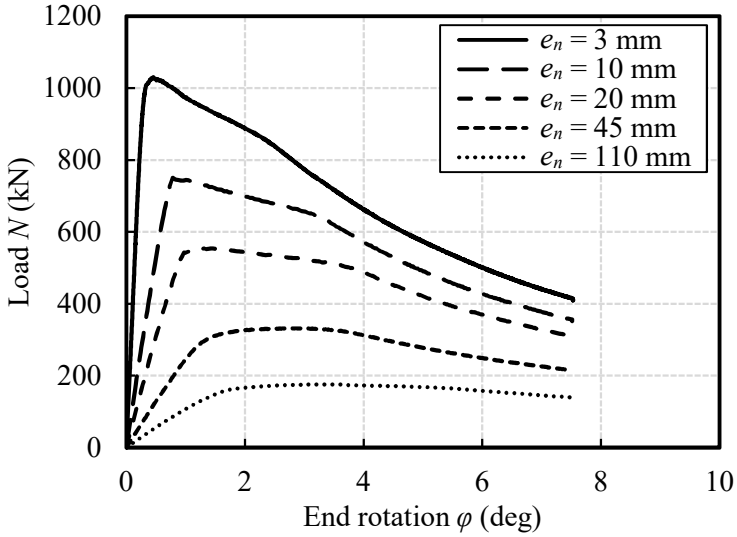
(d) S770 SHS 120×120×6.3 (SSBC5)





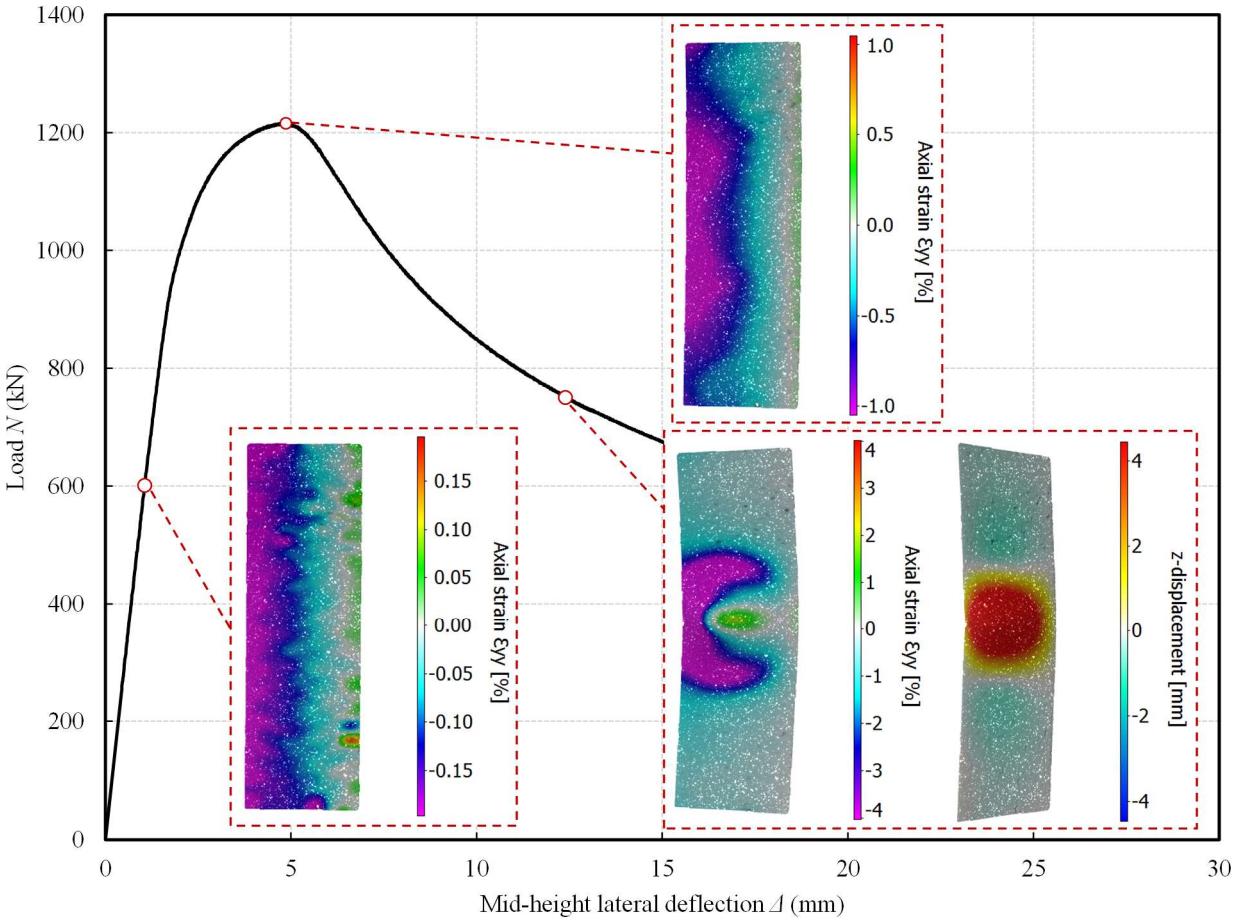
(e) S690 RHS 100×50×5.6 (RSBC1-1 – RSBC1-5, $N + M_y$)



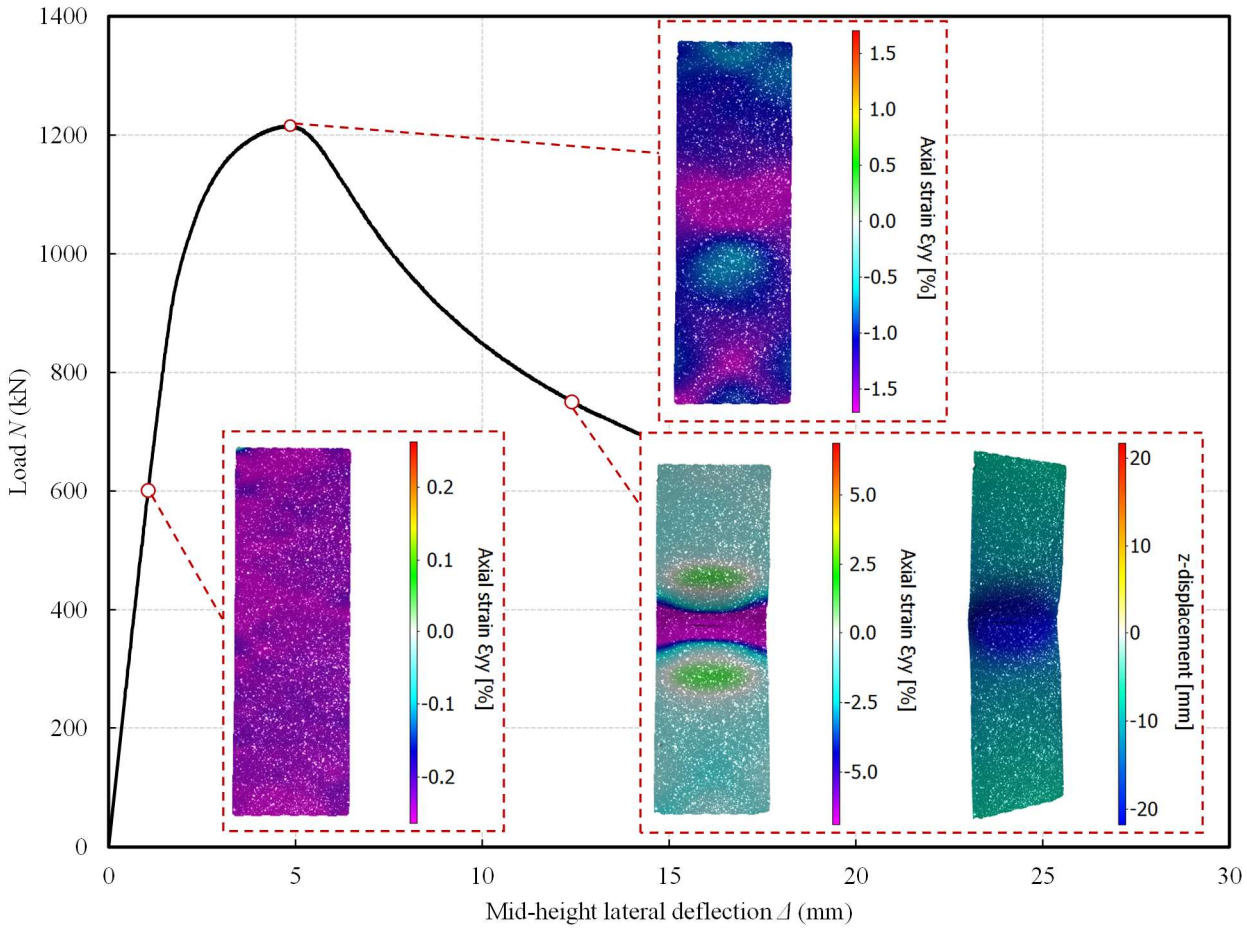


(f) S690 RHS 100×50×5.6 (RSBC1-6 – RSBC1-10, $N + M_z$)

Fig. 15. Load-deformation curves for short beam-column tests: (a) S690 SHS 50×50×5; (b) S690 SHS 90×90×5.6; (c) S690 SHS 100×100×4; (d) S770 SHS 120×120×6.3; (e) S690 RHS 100×50×5.6 ($N + M_y$); (f) S690 RHS 100×50×5.6 ($N + M_z$)


Load N (kN)
Mid-height lateral deflection Δ (mm)
Axial strain εyy [%]
Axial strain εyy [%]
Axial strain εyy [%]
z-displacement [mm]

(a) Side face



(b) Compressive face

Fig. 16. Typical DIC results for short beam-column tests (SSBC5-4): (a) side face and (b) compressive face

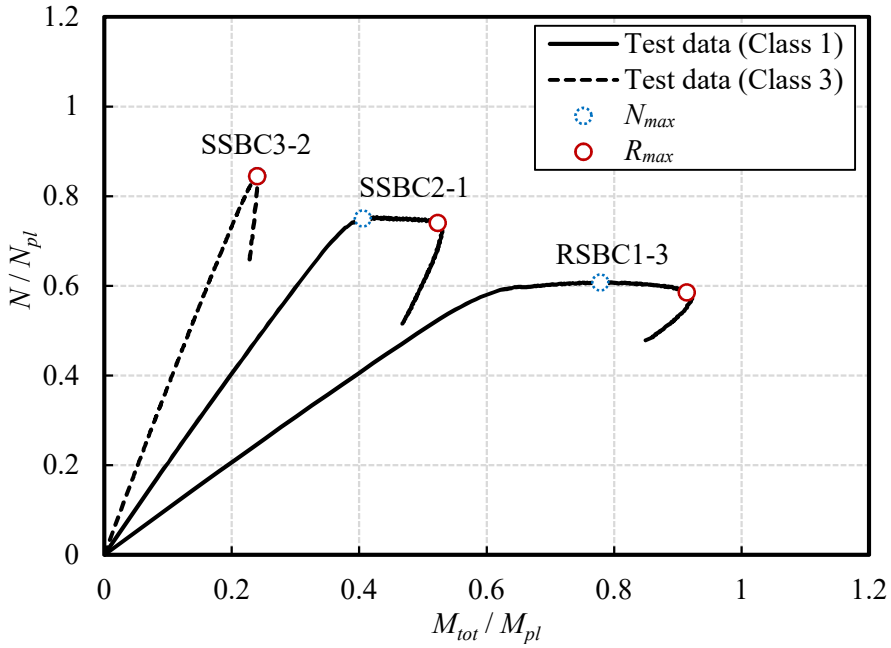
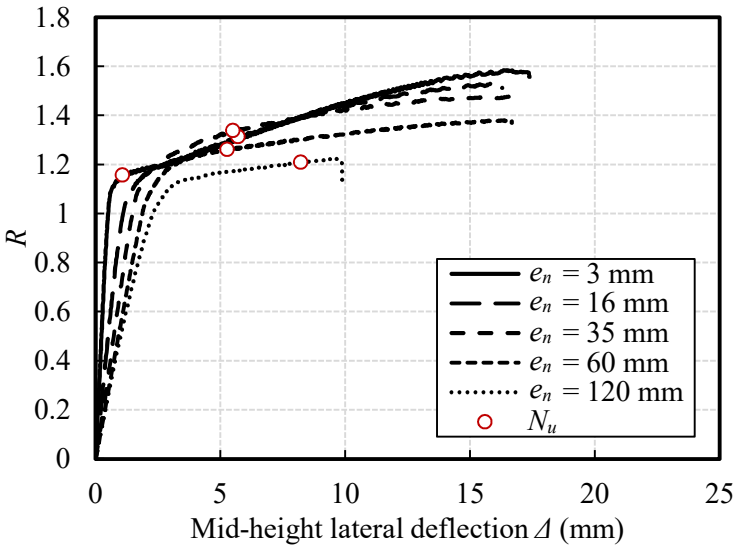
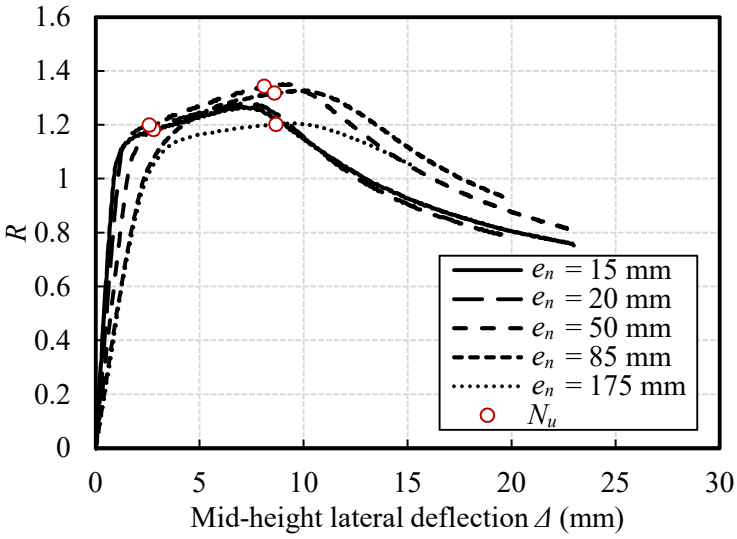


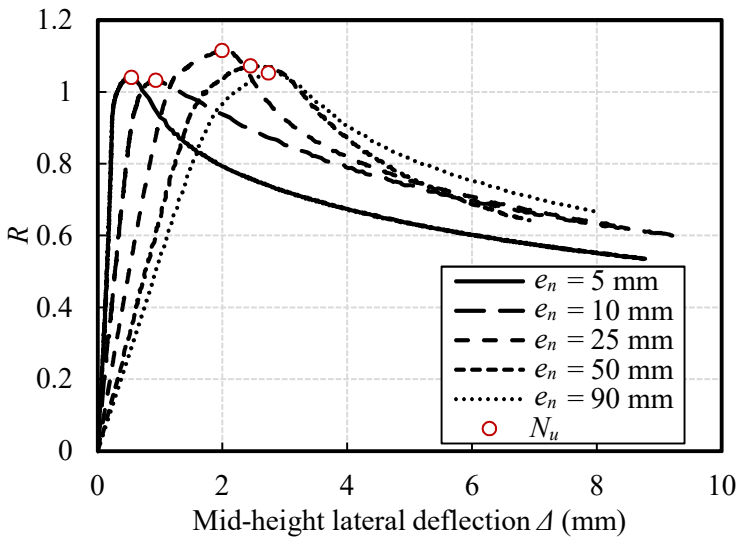
Fig. 17. Characterisation of cross-section failure under combined loading



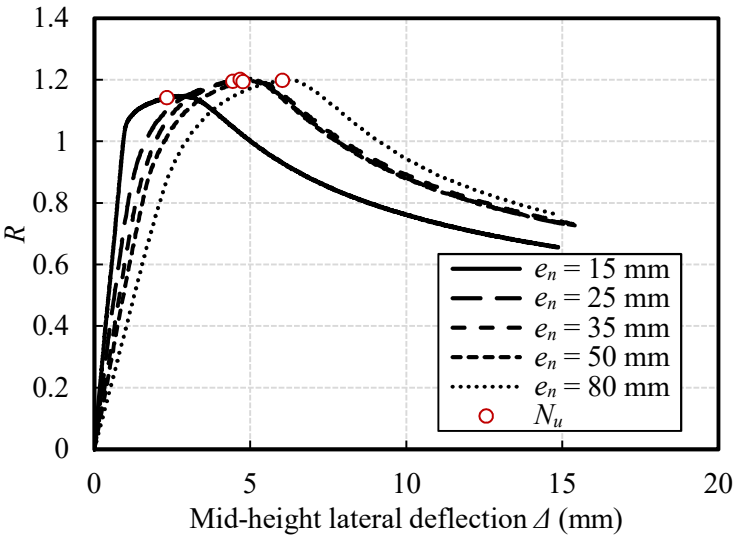
(a) S690 SHS 50×50×5 (SSBC1)



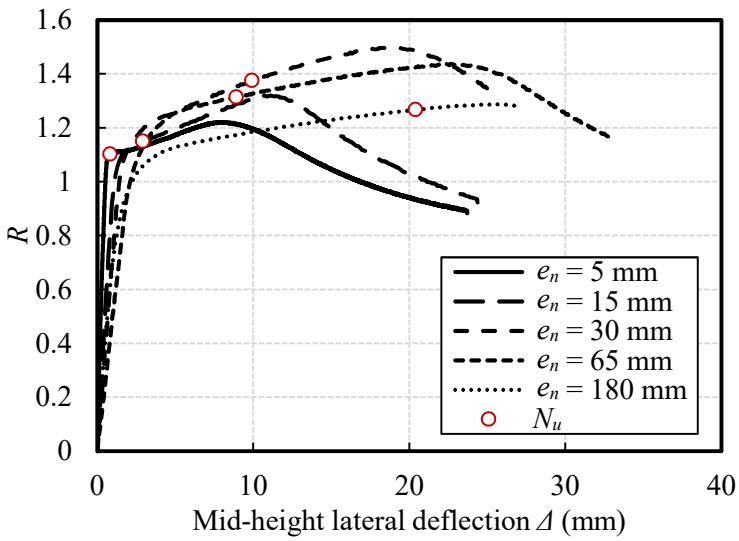
(b) S690 SHS 90×90×5.6 (SSBC2)



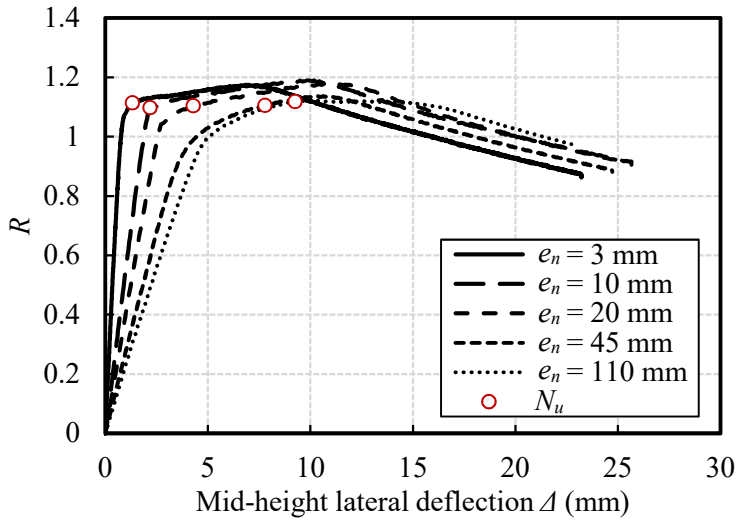
(c) S690 SHS 100×100×4 (SSBC3)



(d) S770 SHS 120×120×6.3 (SSBC5)



(e) S690 RHS 100×50×5.6 (RSBC1-1 – RSBC1-5, $N + M_y$)



(f) S690 RHS 100×50×5.6 (RSBC1-6 – RSBC1-10, $N + M_z$)

Fig. 18. *R*-mid-height lateral deflection curves for short beam-column tests: (a) S690 SHS 50×50×5; (b) S690 SHS 90×90×5.6; (c) S690 SHS 100×100×4; (d) S770 SHS 120×120×6.3; (e) S690 RHS 100×50×5.6 ($N + M_y$); (f) S690 RHS 100×50×5.6 ($N + M_z$)

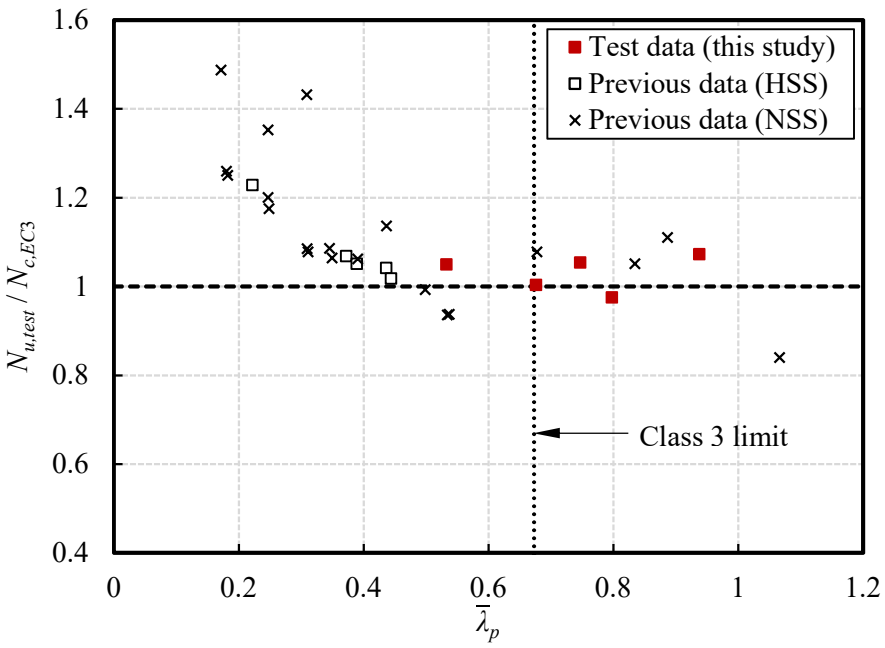


Fig. 19. Comparisons of stub column test data with EC3 design resistance

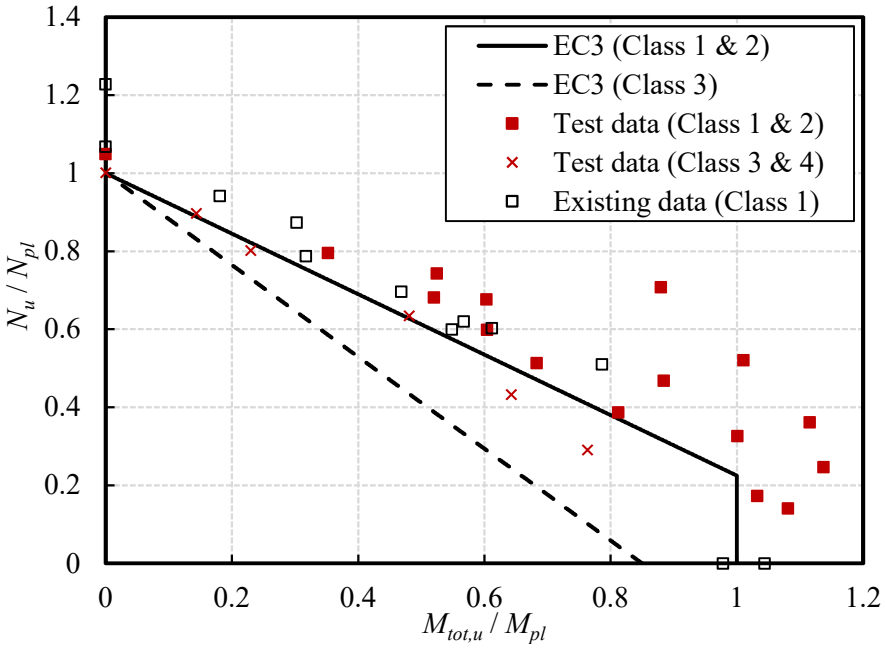
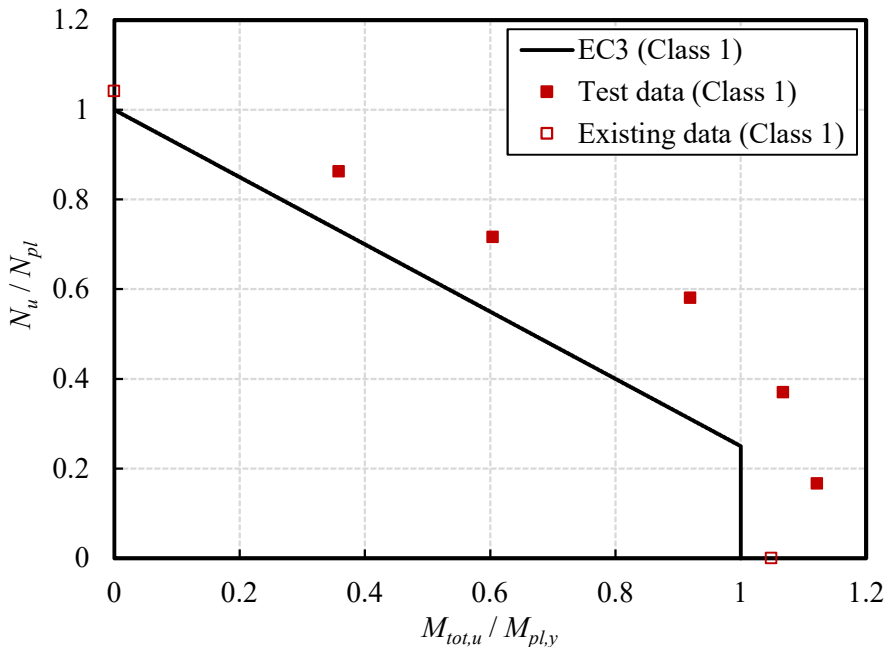
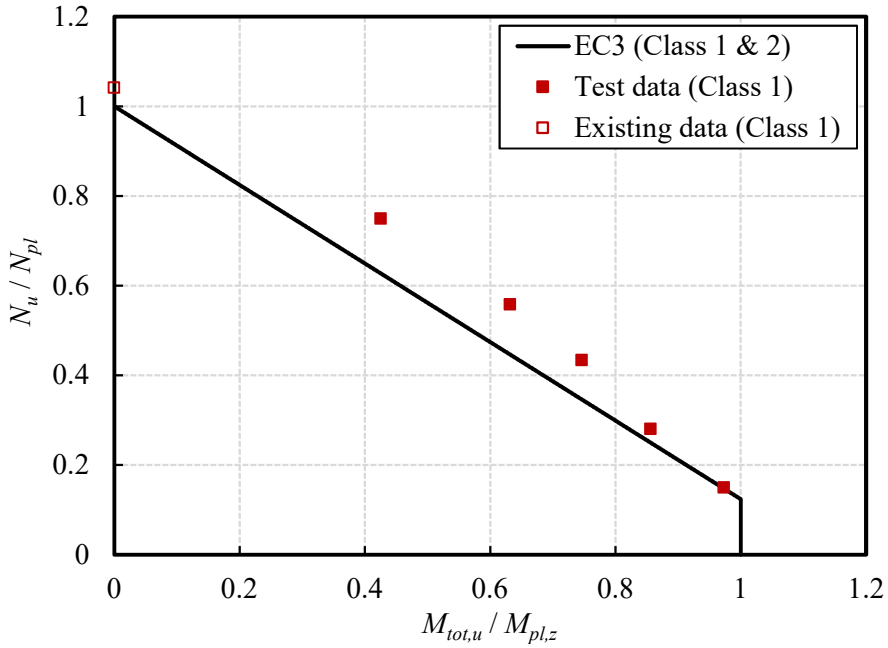


Fig. 20. Comparisons of short beam-column test data with EC3 design curves for SHS



(a) RHS under $N + M_y$



(b) RHS under $N + M_z$

Fig. 21. Comparisons of short beam-column test data with EC3 design curves for RHS under (a) $N + M_y$ and (b) $N + M_z$

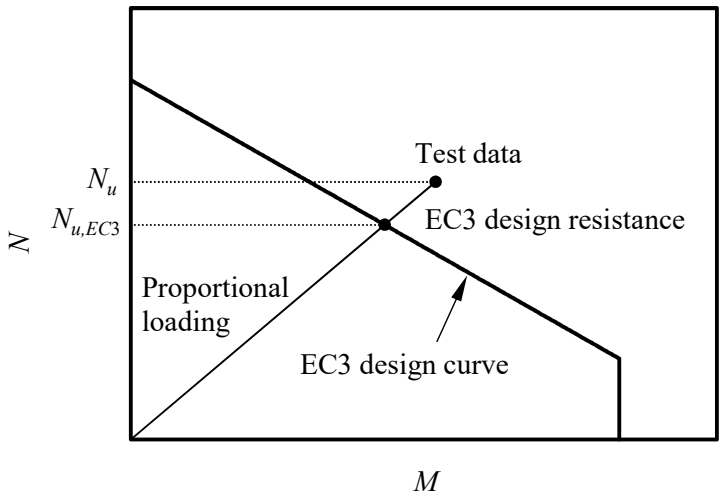


Fig. 22. Definition of N_u and $N_{u,EC3}$ for combined loading